JGR Atmospheres

RESEARCH ARTICLE
10.1029/2022JD036855

Snowband Characteristics Associated With Lake-Effect Misovortices During the OWLeS Project

Scott M. Steiger[1], Matthew Lynne[1], Jake P. Mulholland[2], Karen A. Kosiba[3], and Joshua Wurman[3]

[1]Department of Atmospheric and Geological Sciences, The State University of New York at Oswego, Oswego, NY, USA, [2]Department of Atmospheric Sciences, University of North Dakota, Grand Forks, ND, USA, [3]Department of Atmospheric Sciences, University of Illinois at Urbana-Champaign, Urbana, IL, USA

Key Points:

- Misovortices had preferred locations with respect to lake-effect band centers during the Ontario Winter Lake-effect Systems (OWLeS) project
- Most long lake-axis-parallel lake-effect storms during the OWLeS project had embedded horizontal shear zones leading to misocyclogenesis
- A hypothesis relating these shear zones and their associated misovortices to previously identified low-level boundaries was not supported

Supporting Information:

Supporting Information may be found in the online version of this article.

Correspondence to:

S. M. Steiger,
scott.steiger@oswego.edu

Citation:

Steiger, S. M., Lynne, M., Mulholland, J. P., Kosiba, K. A., & Wurman, J. (2022). Snowband characteristics associated with lake-effect misovortices during the OWLeS project. *Journal of Geophysical Research: Atmospheres*, *127*, e2022JD036855. https://doi.org/10.1029/2022JD036855

Received 4 APR 2022
Accepted 18 AUG 2022

Abstract Vortices of diameters 100 m to 10 km have been observed during lake-effect snowstorms. Lines of misovortices (diameters = 40–4,000 m) have recently been documented forming over Lake Ontario during long lake-axis-parallel (LLAP)-type lake-effect storms. Using National Weather Service Weather Surveillance Radar—1988 Doppler (WSR-88D) and Doppler on Wheels radar data from the Ontario Winter Lake-effect Systems (OWLeS) project, lines of misovortices (also referred to as "misovortex lines" in this study) were investigated for intensive observation period (IOP)7 (7 January 2014) and IOP9 (9 January 2014). Results revealed that the misovortex lines formed on the southern or northern side of the west-to-east-oriented LLAP band, whichever was closest to a low-level boundary nearest the corresponding south or north shoreline (northern part in IOP7, southern part in IOP9). Examination of these two IOPs in the context of a total of 23 OWLeS IOPs, 11 of which had predominantly LLAP band morphology, showed that, in 4 of the 11 LLAP IOPs, horizontal shear zones/reflectivity bands formed in preferred regions over Lake Ontario and nearby land areas where low-level boundaries (e.g., land breeze fronts) have been noted to develop near shoreline irregularities. Horizontal shear zones were predominant in approximately half of the OWLeS LLAP IOPs and were associated with storms having a well-organized, solid banded reflectivity structure. Misovortices occurred when horizontal shear zones were prevalent, supporting the idea that horizontal shearing instability was important to their formation.

Plain Language Summary Previous work has shown lake-effect snowstorm bands that form along the long axis of Lake Ontario develop on/near preexisting low-level boundaries (e.g., land breeze fronts). Multiple local areas of rotation (vorticity) have been observed to form within these bands, especially when using high-resolution Doppler weather radar, and these vorticity centers are associated with heavier precipitation and gustier winds. We test the hypothesis that these small-scale vortices (also known as "misovortices") form due to the low-level horizontal shear associated with the aforementioned boundaries. The hypothesis that horizontal shear zones set the stage for vortex development in these storms is well-supported, but the hypothesis that it is previously identified boundaries that lead to shear zones upon which misovortices form is not well-supported when using data collected from over 20 storm events during the Ontario Winter Lake-effect Systems field project.

1. Introduction

Lake-effect storms develop in different morphologies dependent primarily on lake shape and prevailing steering-level (e.g., 850 hPa) wind speed and direction. Niziol et al. (1995) describe five common morphologies of lake-effect storms across the Great Lakes: (a) wind-parallel bands that form along the long axis of an elliptical lake (also referred to as long lake-axis-parallel [LLAP] bands by Steiger et al., 2013), (b) wind-parallel bands that form when the winds cross the shorter axis of a lake, (c) multi-lake bands, (d) land-breeze induced shore-parallel bands, and (e) mesoscale vortices. The LLAP band is of particular interest to meteorologists due to its propensity to produce heavy snowfall, occasional lightning (Steiger et al., 2018), and lines of misovortices (Kosiba et al., 2020; Mulholland et al., 2017; Steiger et al., 2013; also referred to as "misovortex lines" in this study). The LLAP-type bands occur most frequently over Lakes Erie and Ontario (see Figures 1–3 for lakes' locations) compared to the other Great Lakes, accounting for 32% of lake-effect cases over Lake Ontario as opposed to ~10% over the other Great Lakes (Kristovich & Steve, 1995). The aforementioned LLAP characteristics, hazards, and climatology have motivated field projects over and near Lake Ontario such as done by Peace and Sykes (1966) to the more recent projects described in Steiger et al. (2013) and the Ontario Winter Lake-effect Systems (OWLeS)

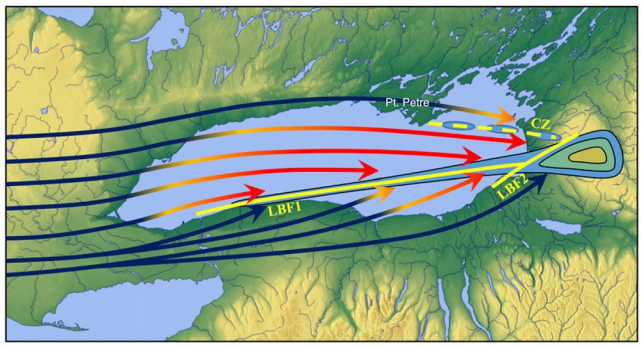

Figure 1. Figure 12 from Steenburgh and Campbell (2017) showing surface boundaries detected during OWLeS IOP2b (11 December 2013) over Lake Ontario: Land Breeze Fronts (LBFs) 1 and 2 and a Convergence Zone (CZ) emanating from Pt. Petre, Ontario, Canada. Airstreams (coloring shows air temperature increases from blue to red) and reflectivity (contoured and shaded) of the LLAP lake-effect band are also shown. LBFs 1 and 2 originate along a "south shore bulge" and the "southeast shore" geographical features, respectively, first identified by Steenburg and Campbell (2017) (note these features are at the respective labeled locations in the diagram). © American Meteorological Society. Used with permission.

project (Kristovich et al., 2017) to improve understanding of the structure and dynamics of these storms. A common lake-effect band structure noted in these studies (especially when analyzing higher resolution Doppler radar data as in Mulholland et al., 2017 and Steiger et al., 2013) is the development of heavy snow and vortices along a distinct low-level boundary.

Using a mesonetwork of surface weather stations, Peace and Sykes (1966) identified a distinct mesoscale boundary within a Lake Ontario LLAP-type snowband along the band's west-to-east major axis. Their Figure 6 shows low-level convergence and inferred cyclonic vorticity along this boundary. A linkage between these mesoscale boundaries and Lake Ontario geographical features was shown in Steenburgh and Campbell (2017). They noted multiple low-level boundaries form under conditions where LLAP snowbands occurred (during intensive observation period [IOP] 2b in the OWLeS project) as westerly airflow interacts with Lake Ontario convex shoreline features. They identified a land-breeze front (LBF) originating from a shoreline "bulge" on the southwestern shoreline, another LBF on the southeastern shoreline, and a convergence zone (CZ, weaker baroclinity compared with the LBFs) associated with Point Petre on the northeastern shoreline (Figure 1). These LBFs are a result of differential diabatic heating and kinematic processes (i.e., convergence via differential surface roughness between land/water) as cold air moves over the relatively warmer waters of Lake Ontario and subsequent advection of these enhanced temperature gradients extend the LBFs tens of km downstream along the long axis of the lake during LLAP events. Similar lake-effect bands associated with these boundaries are discussed by Bergmaier and Geerts (2020) for OWLeS IOPs 7 and 9.

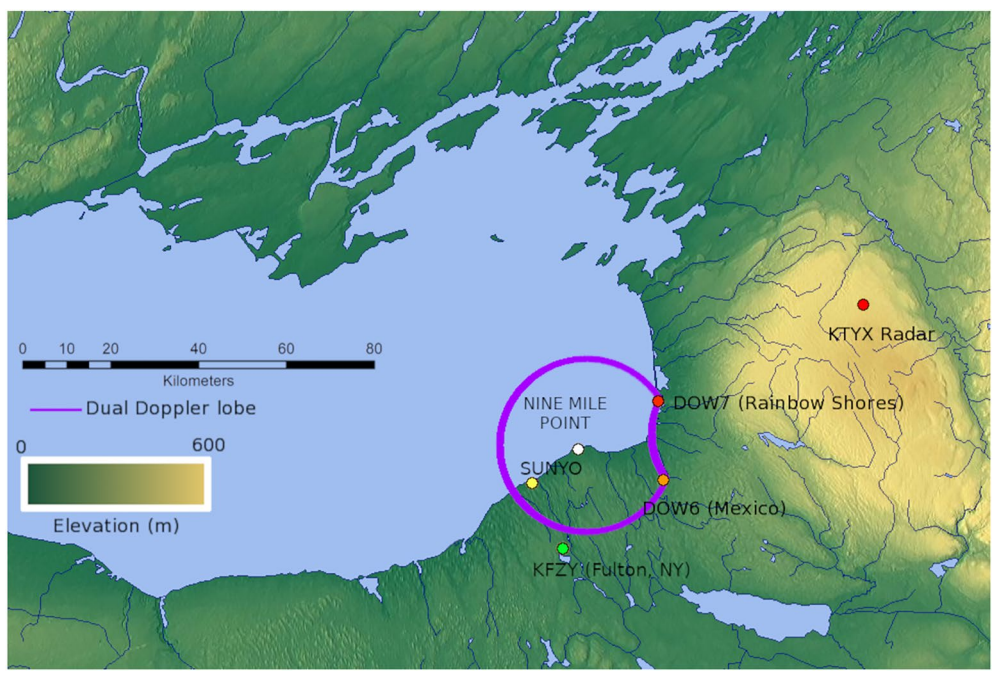

Figure 2. Map of the eastern Lake Ontario region which was the focus of most Ontario Winter Lake-effect Systems (OWLeS) intensive observation periods (IOPs). The Doppler on Wheels (DOW6 and 7) locations and the western dual-Doppler lobe (shown in purple) for the IOP9 (9 January 2014) case study are shown, along with the locations of the nearest WSR-88D radar (KTYX) in Montague, NY, atop the Tug Hill Plateau (50 km to the east-northeast of DOW7 and 400 m above the lake surface), SUNY Oswego (SUNYO), and the Fulton, NY (KFZY), automated surface National Weather Service station. Elevation is shown in meters above sea level.

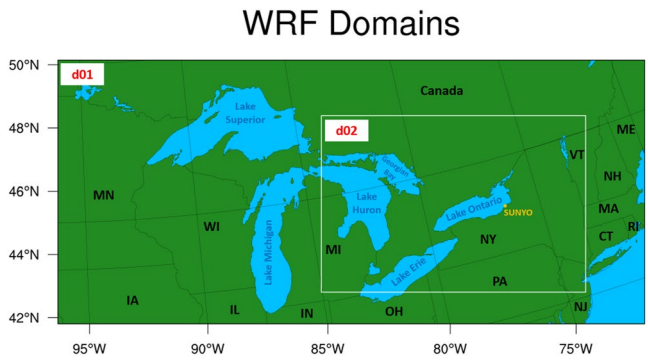

Figure 3. Weather Research and Forecasting (WRF) domains used for simulation of IOP9 (9 January 2014). The outermost domain (d01) had a 3 km horizontal grid spacing and d02 had a 1 km horizontal grid spacing. SUNYO, SUNY Oswego, NY.

During the OWLeS LLAP event IOP7 (7 January 2014), a low-level boundary formed near the location of the CZ identified by Steenburgh and Campbell (2017) and was associated with a cyclonic horizontal shear zone that developed along the northern side of a zonal precipitation band (Mulholland et al., 2017). The shear zone developed in response to a stronger north-to-south horizontal pressure gradient across the southern part of the lake, which created a stronger westerly wind field there as compared to the northern part of the lake (Mulholland et al., 2017). Steiger et al. (2013) discusses the horizontal pressure gradient is enhanced across southern Lake Ontario (west-east-oriented lake) in the case of synoptic-scale westerly flow during lake-effect storms because a zonally elongated surface mesolow (meso-α-scale; Fujita, 1981) forms across the lake, and a smaller scale mesolow (meso-β-scale) forms under the snowband. It has been suggested that the formation of these mesolows may be in response to sensible (forcing the meso-α low) and latent heat (meso-β) fluxes off of the lake surface (Steiger et al., 2013). These pressure fields in turn increase the north-to-south horizontal pressure gradient to the south of the band's precipitation core (i.e., placing lower pressure closer to the synoptic-scale higher pressure to the south of Lake Ontario), creating the stronger westerly winds there and hence a cyclonic shear zone immediately to the north of these stronger westerly winds. The shear zone's vertical vorticity field can then be enhanced by the convergence associated with a boundary. Distinct regions of enhanced vertical vorticity (i.e., vortices) may develop if the shear zone "breaks down" and are further intensified by vortex stretching owing to updrafts within the snowband. Hence, we propose boundaries that form in association with Lake Ontario LLAP bands are sources of cyclonic vertical vorticity and may potentially serve as instigators for vortexgenesis (e.g., Kosiba et al., 2020; Mulholland et al., 2017; Steiger et al., 2013).

The horizontal shear zone along the boundary embedded in an LLAP band analyzed by Mulholland et al. (2017) led to the development of a line of misovortices (diameter 40–4,000 m; Fujita, 1981) on 7 January 2014 (IOP7). A dual-Doppler analysis of this misovortex-bearing snowband coupled with numerical modeling strongly supported that the Lake Ontario misovortices within LLAP bands formed in response to the release of horizontal shearing instability (HSI) along the low-level boundary. Further support for the role of HSI in misovortexgenesis includes that the misovortices were in a line, were somewhat evenly spaced, were of the same sign of vertical vorticity (all cyclonic), and had little interaction (i.e., they did not merge or exhibit a Fujiwhara effect; Fujiwhara, 1931) with maximum vertical vorticity located across the lowest 1 km AGL. The misovortex line formed along a low-level boundary on the snowband's northern side. Similarly, an analysis of a misovortex-bearing snowband in OWLeS IOP4 (15–16 December 2013) yielded comparable misovortex characteristics and support for the role of HSI in their development, although with the notable exception that the location of the line of vortices varied within the snowband throughout the IOP (Kosiba et al., 2020).

Lines of misovortices in Lake Ontario LLAP bands tend to form and persist in certain locations within the reflectivity band and these locations can vary between events and during an event. The OWLeS IOP7 event had a low-level boundary and associated misovortex line on the northern side of an LLAP band (Mulholland et al., 2017) while, in contrast, IOP9 (9 January 2014) had a low-level boundary and misovortex line on the southern side of an LLAP band (to be shown in this paper). The misovortex line's location within the band was variable during IOP4 (e.g., sometimes on the northern/southern side/in the middle; Kosiba et al., 2020). Given the uncertainties of what mechanisms dictate misovortex line placement within LLAP bands, along with the aforementioned knowledge gaps outlined above, we pose the following research questions:

- Why do misovortices and their parent shear zones sometimes have preferred in-band locations in these LLAP storms?
- What is the mechanism for shear zone development within LLAP lake-effect storms and does the release of HSI explain why most misovortices develop in LLAP storms?

This paper presents a detailed comparison (repeating the dual-Doppler and Weather Research and Forecasting [WRF] simulation methodology as done in Mulholland et al., 2017) of the IOP9 lake-effect misovortex event with the IOP7 event documented by Mulholland et al. (2017) due to the distinct differences in misovortex line

placement (opposite sides of a zonally oriented band). We seek to identify the reason(s) why lines of misovortices form in certain lake-effect band regions. Steenburgh and Campbell (2017) identified three low-level boundaries that formed under LLAP conditions across Lake Ontario (two boundaries across southern Lake Ontario and one across northern portions of the lake). We hypothesize that when a lake-effect band develops near one of these boundaries, pre-existing vertical vorticity is enhanced due to convergence along the boundary and vortex stretching associated with the lake-effect band updrafts. A horizontal shear zone first forms due to the pressure-wind field shown to set up during an LLAP event in Mulholland et al. (2017). The enhanced vertical vorticity along the shear zone develops on the band's side closest to one of the Steenburgh and Campbell (2017) boundary locations (e.g., the north side of the band if the band forms on the northern lake side close to the CZ) and sets the stage for the release of HSIs and a line of misovortices to form. We test this hypothesis by analyzing operational National Weather Service and research (e.g., Doppler on Wheels [DOW]) radar data for the band's reflectivity core and shear zone's proximity to where the Steenburgh and Campbell (2017) boundaries develop. We hypothesize that when a misovortex line forms on the northern side of an LLAP band, as during IOP7, that this line was forced by a boundary similar to the Point Petre CZ, and when the misovortex line forms on the southern side of an LLAP band, as during IOP9, it was forced by a boundary similar to one of the southern Lake Ontario LBFs as identified by Steenburgh and Campbell (2017).

Section 2 discusses the data and methods used to analyze IOP9 and to place this along with IOP7 in the context of other OWLeS cases. Section 3 compares dual-Doppler radar analyses for IOP9 to similar analyses done for IOP7 by Mulholland et al. (2017) to show the relative positions of vortex lines. This section also includes model analyses of these IOPs to understand the origin of the boundaries upon which misovortices formed in these cases. We then expand these results to other LLAP bands with and without misovortices by examining radar mesoscale characteristics (e.g., presence of shear zones) of all events during OWLeS in Section 4. Section 5 discusses potential reasons for why these misovortices form in certain positions within LLAP bands and Section 6 will have concluding remarks.

2. Data and Methods

2.1. DOW Radar Analysis of IOP9

Dual-Doppler radar analyses were conducted using data collected by two DOW (Wurman et al., 2021) X-band radars (DOWs 6 and 7) during IOP9 on 9 January 2014 between 04:30 and 06:30 UTC (Wurman & Kosiba, 2018). During OWLeS, the DOWs used 60 m range gates, the 0.93°-beamwidth was indexed at 0.5°, and a staggered pulse repetition time resulted in a ∼79 m s^{-1} Nyquist velocity. The radar locations and the pertinent dual-Doppler lobe are shown in Figure 2. DOW6 was deployed just east of Mexico, NY (43.4670°N, 76.1742°W, 40 m above lake level), and DOW7 was deployed at Rainbow Shores, NY (43.6142°N, 76.1979°W, on lakeshore). The DOW radar data editing and analysis methods were nearly identical to those described by Kosiba et al. (2013) and Mulholland et al. (2017). To summarize here, raw data were edited using SOLO3 software with data east of the 15 km south-north baseline between the two radars removed due to substantial beam blockage (hence why only the western dual-Doppler lobe is shown in Figure 2). Ground/sea clutter was removed using a cross-correlation coefficient minimum threshold of 0.94.

Edited radar data were objectively analyzed to a $40 \times 40 \times 2.7$ km^3 Cartesian grid using a two-pass Barnes scheme (Barnes, 1964). A horizontal and vertical grid spacing of 270 m was chosen based on Δx, Δy, $\Delta z = 5\delta/12$, where $\delta = (\theta)\,(\pi/180°)\,(X)$. X is the farthest distance (km) from the radars to a feature of interest (i.e., a misovortex in this study, 40 km) and θ is the beamwidth. An isometric Barnes smoothing parameter (κ) of 0.747 km^2 and a second pass convergence parameter (γ) of 0.3 was used (Majcen et al., 2008; Pauley & Wu, 1990). Three-dimensional wind analyses were obtained from the objectively analyzed radar data by integrating the anelastic mass continuity equation upward from the domain bottom (assuming vertical velocity = 0 m s^{-1} at the lower boundary) using software provided by the Center for Severe Weather Research (CSWR, 2020).

2.2. WRF Model Simulations of IOPs 7 and 9

Weather Research and Forecasting (WRF-ARW; version 3.7.1; Skamarock et al., 2008) model simulations were conducted for IOPs 7 and 9 to aid in identifying mesoscale boundaries and their formation characteristics (e.g., baroclinity) over and near Lake Ontario that influence misovortexgenesis as low-level observations that would be

Table 1
Summary of 9 January 2014 (IOP9) WRF Model Specifications

	Specification	Reference (if necessary)
Horizontal grid spacing	3 km (d01); 1 km (d02)	–
Number of vertical levels	60	–
PBL scheme	Shin-Hong	Shin and Hong (2015)
Microphysics scheme	Thompson	Thompson et al. (2008)
Radiation scheme	RRTMG	Iacono et al. (2008)
Surface layer scheme	MM5 similarity theory	Jiménez et al. (2012)
Land surface model	Noah	–
Cumulus scheme	None	–

used to analyze the boundaries were very limited on the land near the lake and non-existent over the lake. Details regarding the WRF simulation for IOP7, which is similar to what is outlined below for IOP9, can be found in Mulholland et al. (2017). The main difference between the WRF simulations of these two IOPs were the different regional models used to initialize the lateral boundary conditions of the outer grids every 6 hr (IOP7 = 13 km Rapid Refresh [RAP] model initialized at 00 UTC 7 January 2014; IOP9 = 12 km North American Mesoscale [NAM] model initialized at 00 UTC 9 January 2014). This difference was necessary in order to produce the most realistic model depiction of each IOP's LLAP band. Specifically, for the IOP9 WRF simulation, a 1 km horizontal grid spacing domain (d02; 901 × 601 grid points; Figure 3) was nested within a 3 km horizontal grid spacing domain (d01; 667 × 300 grid points; Figure 3). Model output was saved at a frequency of every 1 hr for the 3 km domain and 30 min for the 1 km domain. The 3 km domain was used to capture the eastward-moving upper-level trough across the Great Lakes which occurred in both IOPs (see Section 3.1 for IOP9 discussion) while the 1 km domain was used to simulate boundaries similar to the low-level LBFs and CZs across Lake Ontario as described by Steenburgh and Campbell (2017). The model simulation used 60 vertical levels with a terrain-following sigma coordinate and a vertically stretched grid. The top of the model domain was at 50 hPa (~20 km AGL). A dampening layer was implemented across the uppermost 5 km of the model domain. A complete outline of the model specifications, including parameterization schemes (which are similar to those used in Steenburgh & Campbell, 2017), is found in Table 1.

2.3. Classification of Band Radar Characteristics During All OWLeS IOPs

We examined the presence/absence, location, and morphology of a shear zone for all the lake-effect events observed during OWLeS to contextualize the shear zone and misovortex line characteristics of IOPs 7 and 9. The goals were to determine if there were common conditions under which misovortices developed in these storms and to give support for the hypothesis that boundaries associated with Lake Ontario shoreline features (e.g., similar to the LBFs and CZ in Steenburgh & Campbell, 2017) are vital to the development of misovortex lines in LLAP bands.

2.3.1. Lake-Effect Storm Morphology and Banding Type

Following Veals and Steenburgh (2015), lake-effect storm morphology was identified manually for each OWLeS IOP using the following six categories (Figure 4): (a) LLAP—one or two intense wind-parallel (e.g., within boundary layer at 850 hPa) bands formed along the long axis of Lake Ontario (west-to-east) and storm cells extended inland at least 20 km, (b) Broad Coverage—multiple wind-parallel bands generally formed under short fetch (i.e., the distance air travels over water) conditions, (c) Hybrid—combination of LLAP and Broad Coverage, (d) Mesoscale Vortex—storm characterized by broad rotation, (e) Lake-Orographic—stationary heavy concentration of radar echoes over the Tug Hill Plateau, and (f) Shoreline—land-breeze-induced storms that formed very close to the shoreline and do not penetrate more than 20 km inland. Weather Surveillance Radar—1988 Doppler (WSR-88D) base (0.5° elevation angle) reflectivity data collected at Montague, NY (KTYX, Figure 2), were consulted every 10 min, similar to Kosiba et al. (2020) in their multi-case study, for the duration of an IOP and the appearance of the band in the radar data was matched to a morphological type. Note these base-level radar data were ~1.0 km AGL over the east-central Lake Ontario shoreline. Level-II reflectivity data from the

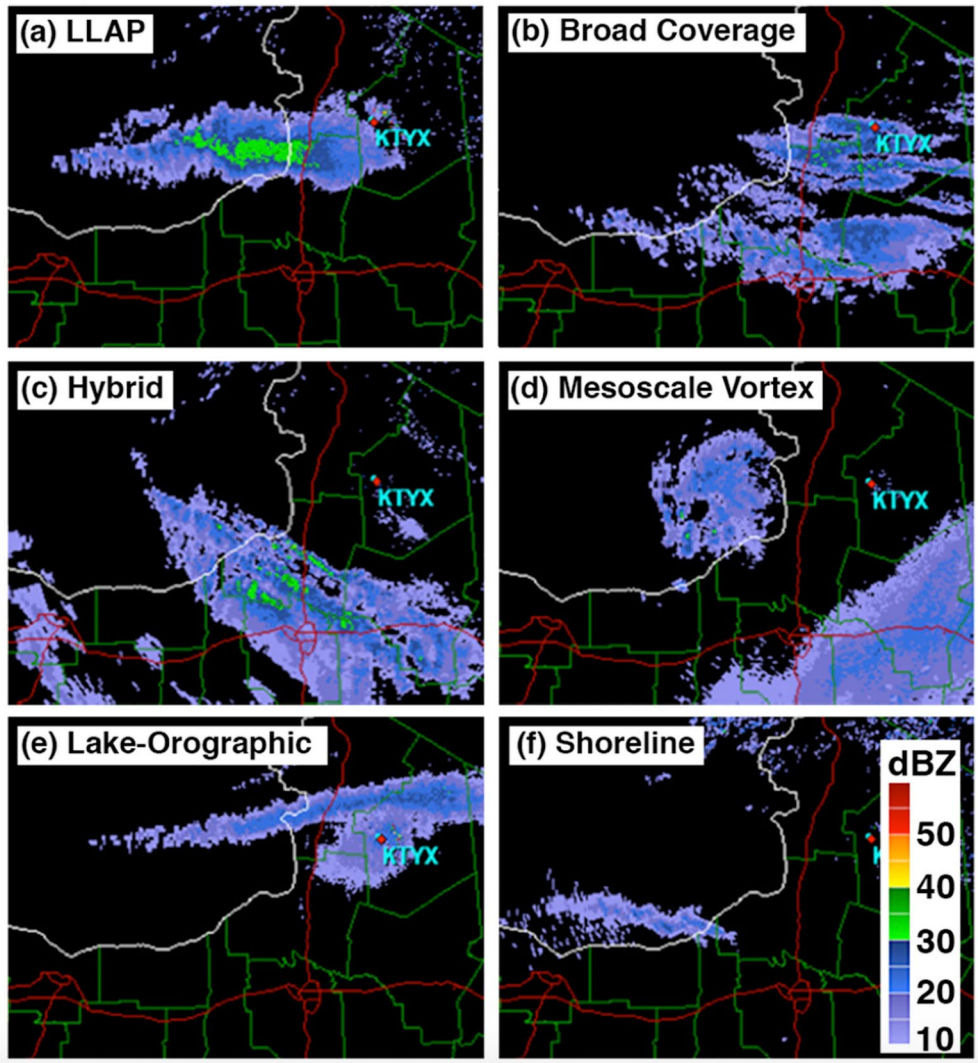

Figure 4. The morphological types of Lake Ontario lake-effect storms as defined by Veals and Steenburgh (2015, Figure 2 reproduced here) based on typical patterns detected by 0.5° angle (base) WSR-88D KTYX radar reflectivity (dBZ) scans. © American Meteorological Society. Used with permission.

National Centers for Environmental Information (NCEI) were analyzed using the NOAA Weather and Climate Toolkit (NCEI, 2022). As this paper is concerned with features (i.e., misovortices) that occur mostly in LLAP lake-effect systems (e.g., Steiger et al., 2013), only the periods when the morphological type was LLAP were further considered. Some hybrid and lake-orographic events were included with LLAP events as they can have characteristics of LLAP systems. As such, they could potentially contain shear zones and misovortices the same as a pure LLAP system.

Predominant event banding type was also identified manually (every 10 min of an LLAP IOP), following a modified version of the process described in Campbell et al. (2016), in order to explore whether or not shear zones and/or misovortices only form when lake-effect bands are characterized by regions of continuous reflectivity, or if they can also form in association with more cellular band types. The banding type was analyzed along the axis of highest reflectivity during a period of LLAP lake-effect morphology. For a system to be classified as "banded," the radar echoes along the axis of highest reflectivity must have continuous (on the order of tens of km) reflectivity ≥20 dBZ organized in a linear fashion. To be classified as "weakly banded," the radar echoes must have been individual cells of ≥20 dBZ connected by regions of weaker radar echoes (<20 dBZ) and must have been

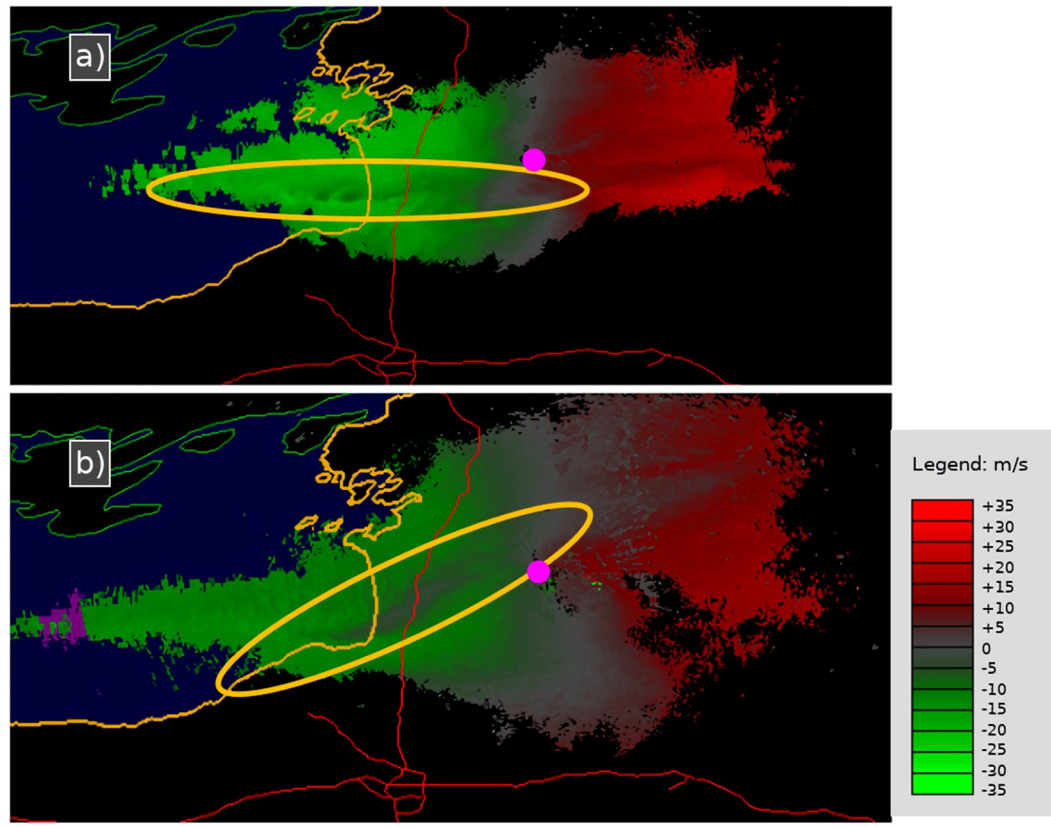

Figure 5. KTYX radial velocity (m s^{-1}) imagery showing horizontal shear zones during (a) OWLeS IOP4 (16 December 2013) at 04:07 UTC (strong and distinct shear zone [yellow oval]) and (b) IOP9 (9 January 2014) at 05:18 UTC (a much weaker and less distinct shear zone [yellow oval]). The radar's location is at the magenta dot (embedded within the data) to the east of the lake.

arranged linearly. "Non-banded" periods had cells with reflectivity ≥20 dBZ that had no discernible reflectivity (≥0 dBZ) connecting them.

2.3.2. Identification of Shear Zones and Misovortices

As misovortices have been found along low-level horizontal shear zones that extend along the major axes in LLAP lake-effect systems, identifying the presence of this major shear zone is a likely first step in identifying the presence of misovortices (Kosiba et al., 2020; Mulholland et al., 2017; Steiger et al., 2013). Quasi-linear horizontal shear zones (e.g., Figure 5) were manually identified by examining KTYX base radial velocity imagery every 10 min of an LLAP IOP. The shear zone was defined as a continuous linear feature of abrupt azimuthal/radial shear (e.g., Figure 5) that extended ≥25% of the band length along its major axis or ≥10 km (= 2.5 x the maximum misovortex diameter as defined by Fujita, 1981). If a shear zone was only present close to the surface (<1 km AGL), it was likely the KTYX radar did not detect it. To reduce missing a near-surface shear zone, DOW data (when available), which were collected closer to the surface, were also manually analyzed when shear zones were not apparent on KTYX imagery. Any major shear zone was then investigated for evidence of misovortices (i.e., velocity couplets in lowest, unblocked elevation angle DOW data or KTYX data when DOW data were not available).

The locations of shear zones and misovortex lines relative to the reflectivity core of the zonally oriented LLAP band were manually classified every 10 min into the following categories: north, middle, south, or transected the band from north to south or south to north. We next noted if LLAP reflectivity bands and/or shear zones as viewed with KTYX, Buffalo, NY WSR-88D (KBUF), and/or DOW data were "connected" (i.e., any point of the band/shear zone was within 5 km) to the geographical feature ("south shore bulge," "southeast shore," and "Point Petre," in Figure 1) that produced the LBFs and CZ first identified by Steenburg and Campbell (2017)

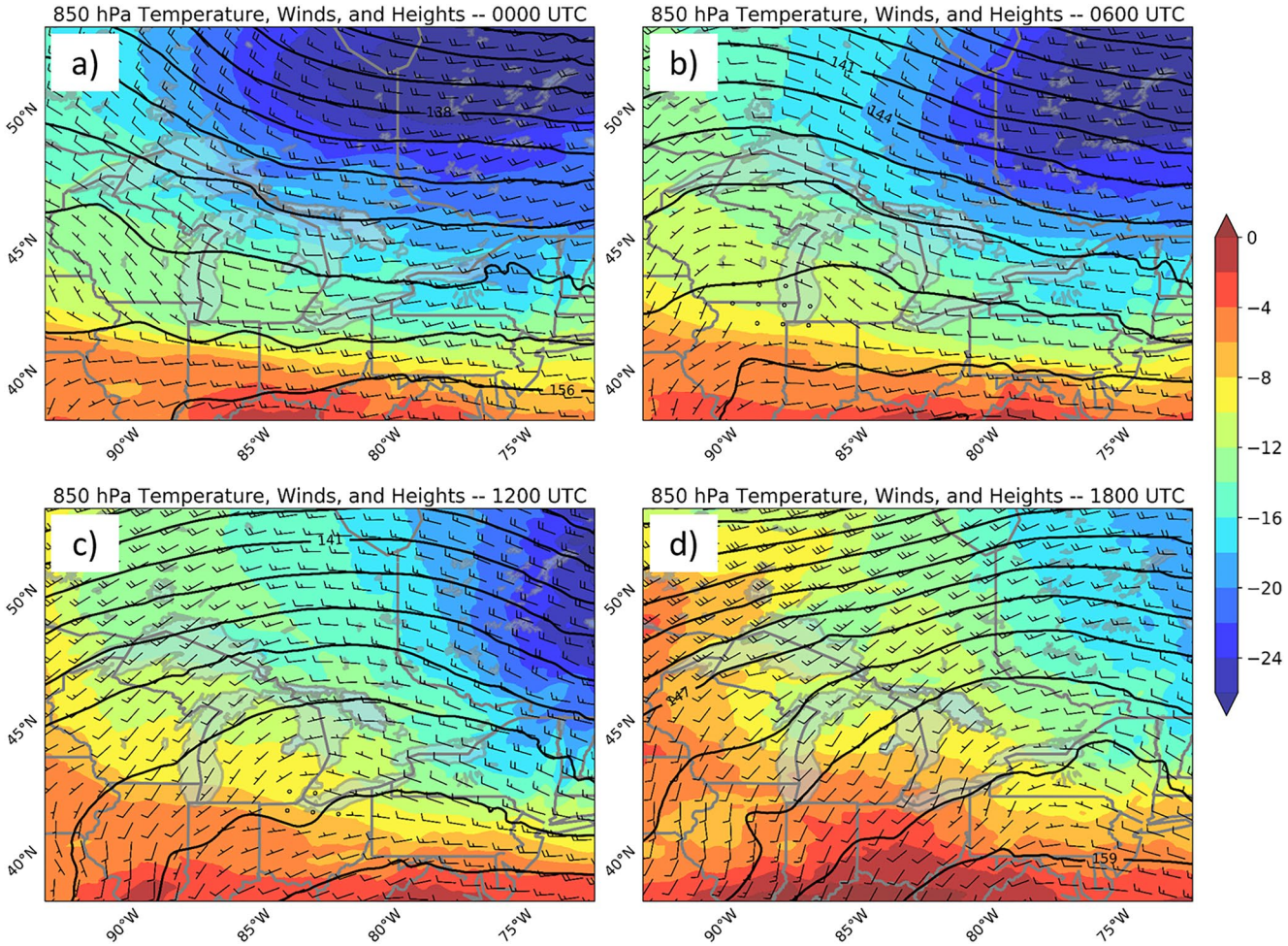

Figure 6. 00 UTC 9 January 2014 12 km NAM model output for the Great Lakes region during IOP9 of 850 hPa horizontal wind (half barb = 5 m s^{-1}; full barb = 10 m s^{-1}), temperature (°C; color shaded), and geopotential height (black contours every 3 dam). Forecast times are at (a) 00, (b) 06, (c) 12, and (d) 18 UTC 9 January 2014.

during OWLeS IOP2b. These reflectivity bands/shear zones also had to be along the same orientation/bearing (within+/−20°) of these boundaries. For example, the bearing of a band should be 225° (coming from the southwest) +/−20° as well as be within 5 km of the southeast shoreline for it to be associated with a boundary similar to LBF2 (Figure 1).

3. Case Analysis

3.1. IOP9 Event Overview

A positively tilted 500 hPa trough axis was located across the upper Great Lakes with the entrance region of a 300 hPa jet streak over Lake Ontario at 00 UTC 9 January 2014. The trough moved southeastward and crossed Lake Ontario around 09 UTC per the 00 UTC operational NAM forecast system (not shown). At 06 UTC the 850 hPa temperature was near −18°C, resulting in a difference with the lake surface temperature (per the Great Lakes Environmental Research Lab database; GLERL, 2022) near 21°C. The 850 hPa wind was westerly at 10–15 m s^{-1} across Lake Ontario, providing a favorable fetch for an LLAP band (Figure 6b). The boundary layer was nearly saturated and extended vertically to ~800 hPa per an OWLeS sounding launched from the State University of New York (SUNY) at Oswego campus into the band at 07 UTC (Figure 7, cf. Figure 2). The boundary layer was defined as the layer in which the atmosphere was well mixed (temperature profile nearly statically neutral) from the ground up to a level where the atmosphere became much more stable (e.g., an inversion). The 850 hPa wind direction veered across Lake Ontario from ~260° at 00 UTC to ~290° at 12 UTC, a reflection of

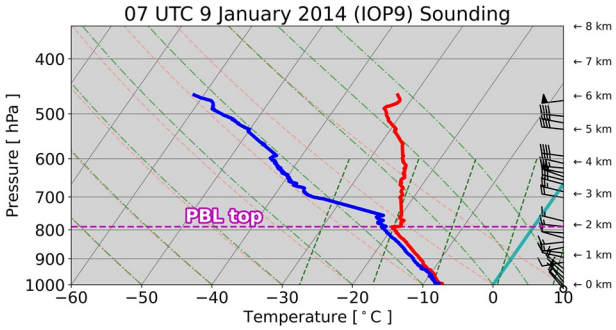

Figure 7. Sounding (plotted on a skew-T, log-P diagram) launched from the SUNY Oswego campus (location shown in Figure 2) at 07 UTC 9 January 2014 into the LLAP band (IOP9). The red line is temperature (°C), the blue line is dewpoint temperature (°C), and horizontal winds are in black barbs (half barb = 5 m s^{-1}; full barb = 10 m s^{-1}; pennant = 25 m s^{-1}). The top of the planetary boundary layer (PBL; see text for definition) is denoted as a horizontal dashed magenta line ~800 hPa. The environmental 0°C line is denoted by the bold cyan line. Altitudes are listed along the right-hand-side of the figure.

the upper-level trough passage and the approach of a low-to-midlevel ridge (Figures 6a–6c). Surface winds also veered from southwesterly to northwesterly around 07 UTC at Fulton, NY (KFZY, near the southeastern corner of Lake Ontario, see Figure 2 for location).

The IOP9 lake-effect band was weakly organized at 00 UTC 9 January, but became an LLAP band with a zonal orientation across northern Lake Ontario by 03 UTC per the KTYX radar (Figure 8a). The band shifted south between 03 and 07 UTC and by 08 UTC manifested as a smaller area of moderate reflectivity (~20–25 dBZ) near the southeastern Lake Ontario shoreline (Figure 8d). The band weakened to scattered light snow showers by 10 UTC after the upper-level trough passed through the area. The LLAP band was most organized and intense (greatest reflectivity and well-banded) during the 05–06 UTC period. A line of misovortices was also most apparent during this time period of maximum intensity along the southern edge of the LLAP band and will be the focus of the next section.

3.2. Single- and Dual-Doppler Radar Analyses of Shear Zones and Misovortices During IOP9

Figure 9 shows the evolution of the KTYX base reflectivity and Doppler radial velocity for a time period when misovortices were most apparent in the DOW6 and 7 radar data (05:12–05:41 UTC). The band was mostly steady state during this period (i.e., similar position and intensity) and had maximum reflectivity between 30 and 35 dBZ ~10 km inland across northern Oswego County, immediately east of Lake Ontario (Figures 9a and 9b). An area of near 0 m s^{-1} radial velocity was embedded within the incoming westerly velocity from near Nine Mile Point (the convex shoreline feature just east of SUNY Oswego, cf. Figure 2) inland to the northern Oswego County border region at the times shown (Figures 9c and 9d). We infer this is an indication of a boundary due to the abrupt change of the shear over a short horizontal distance (~10 km) in the Doppler velocity data and based on its similar shape and location in relation to LBF2 identified in Steenburgh and Campbell (2017) (Figure 1). This possible LBF coincided with the area of greatest reflectivity (Figures 9a and 9b), suggesting that the enhanced low-level convergence along the boundary fostered greater snowfall rates locally.

Near the boundary identified using KTYX observations (cf. Figures 2, 9, and 10), a cyclonic horizontal shear zone occurred along the southern side of the IOP9 LLAP band with couplets of local minima and maxima radial velocity embedded, indicating misovortices (at 05:17 UTC 9 January, see Figure 10) noted in the higher resolution DOW data. The corresponding reflectivity image in Figure 10 shows a scalloped pattern along the south edge of the band likely due to the advection of hydrometeors around the misovortices. The dual-Doppler analysis reveals a line of misovortices (identified as circularly closed contours of vertical vorticity local maxima) was evident along the southern side of the band between 05 and 06 UTC and between 2 and 14 km north of DOW6 (Figures 11 and 12). The shape of the misovortex line mirrored the southeastern Lake Ontario coastline and coincided well in terms of location and shape with the likely LBF indicated in the KTYX radial velocity field (Figures 9c and 9d). The IOP9 band slowly moved southward throughout the period, with four-to-seven misovortices occurring within the dual-Doppler domain at any one time (Figures 11 and 12).

A low-level boundary with misovortices is clearly evident in the dual-Doppler-derived ground-relative horizontal wind field at 05:10 UTC (Figure 11a) along the latitudinal position near 10 km north of DOW6. This low-level boundary persisted throughout the period as it moved southward (Figures 11 and 12). Northwesterly winds (≤10 m s^{-1}) were located north of the boundary within greater reflectivity, while stronger westerly winds (>10 m s^{-1}) existed to the south of the boundary within weaker reflectivity.

3.3. WRF IOP9 Storm Characteristics

A WRF simulation (Section 2.2) was used to better understand how and why a low-level boundary developed within the lake-effect band upon which misovortices formed during IOP9. This boundary can provide the horizontal shear (for HSI) and lift to enhance vertical vorticity via stretching and produce misovortices. The observed

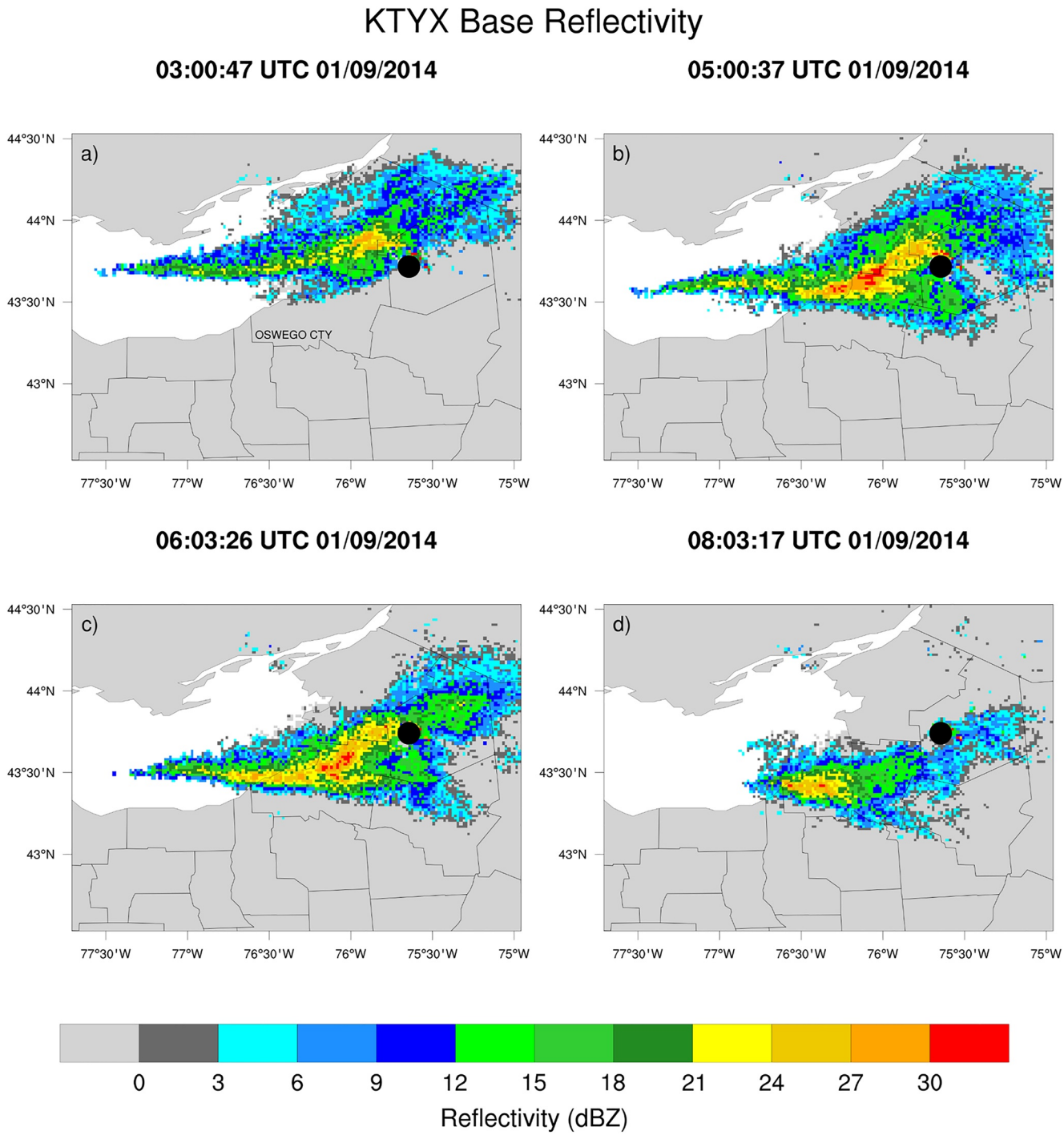

Figure 8. Radar base (0.5° elevation angle) reflectivity (dBZ) at (a) 03:01, (b) 05:01, (c) 06:03, and (d) 08:03 UTC 9 January 2014 (IOP9) from the KTYX WSR-88D (black dot). County outlines are also shown (Oswego County is labeled immediately southeast of Lake Ontario in panel a).

low-level boundary was denoted as a linear wind shift line that did not propagate away from the area of maximum reflectivity (Figures 11 and 12); hence, it was likely not band-generated (e.g., an outflow boundary created by low-level sublimational cooling), but could have been band-enhanced through latent heating and resultant solenoidal secondary circulations (as in Bergmaier & Geerts, 2020 and Bergmaier et al., 2017). A band of convergence originated over southwestern Lake Ontario (over the geographical feature, Steenburgh & Campbell, 2017, term the "south shore bulge") in the WRF simulation and extended eastward across the lake, intersecting another

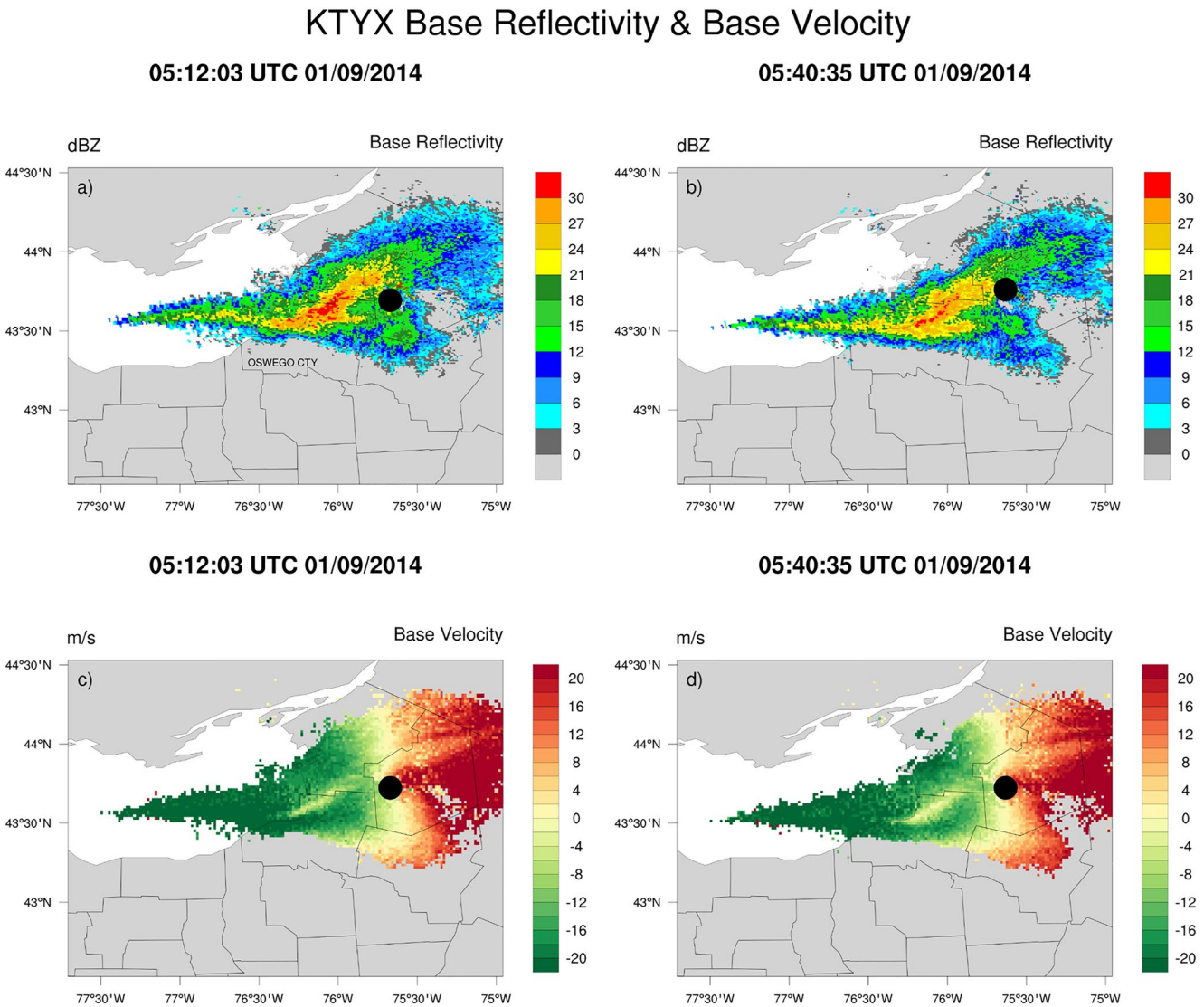

Figure 9. Base reflectivity (dBZ; top panels) and radial velocity (m s^{-1}; bottom panels) at (a, c) 05:12 UTC and (b, d) 05:41 UTC 9 January 2014 (IOP9). County outlines and labels as in Figure 8. These are near the beginning and ending times of when misovortices were most apparent during this IOP.

region of convergence that extended northwest-to-southeast just west of Point Petre, Ontario, Canada (Figure 13). The low-level convergence was greatest, near 1×10^{-3} s^{-1}, to the east of where these two boundaries met, under the lake-effect band, and then along the southeastern shoreline. This low-level convergence pattern was persistent between 04:30 and 06:00 UTC (Figure 13). The persistent wind pattern at the southeast corner of Lake Ontario displayed cyclonic curvature which likely worked in concert with the shear vorticity (stronger zonal winds to the south of the band) to create substantial cyclonic vertical vorticity in the area of the observed misovortices in this case. This curvature vorticity is also apparent in the dual-Doppler analyzed winds (Figures 11 and 12).

In order to elucidate the reasons for the low-level boundary formation underneath these bands, we calculated frontogenesis consistent with the equations presented in Steenburg and Campbell (2017). The diabatic frontogenesis terms were of at least an order magnitude smaller than the kinematic frontogenesis term (not shown), and thus, we only analyze kinematic frontogenesis hereafter. The kinematic frontogenesis pattern (Figure 14) is similar to that shown in Figure 9c in Steenburg and Campbell (2017), with enhanced kinematic frontogenesis in the same areas as the low-level convergence (Figure 13) and LBFs 1 and 2 (Figure 1; Steenburgh & Campbell, 2017). The high spatial correlation between low-level convergence (Figure 13) and kinematic frontogenesis (Figure 14) supports that kinematic frontogenesis was the key aspect as to why these low-level boundaries formed. The main difference

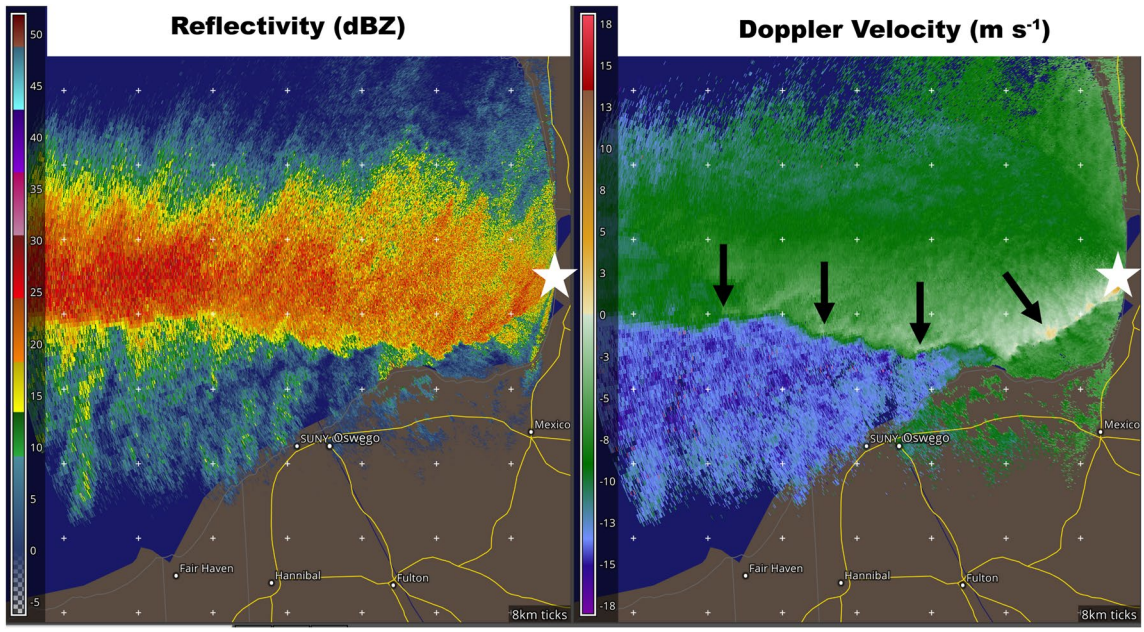

Figure 10. DOW7 reflectivity (dBZ; left) and Doppler velocity (m s^{-1}; right) from the 0.7° elevation scan at 05:17 UTC 9 January 2014 (IOP9). Tick marks are every 8 km and black arrows on the velocity image indicate couplets suggestive of misovortices. The DOW7 location is shown with a white star.

between the conceptual model of boundaries shown in Figure 1 and the similar boundaries which occurred during IOP9 was that the enhanced convergence and kinematic frontogenesis just to the west of Point Petre were likely associated with a boundary similar to an LBF (not just a CZ) based on the magnitude of the potential temperature gradient being similar to that near the LBF 1 and 2 positions (see green contours in Figure 14). Based on this simulation, the IOP9 misovortices likely formed along low-level boundaries (with enhanced convergence and kinematic frontogenesis) similar to LBFs 1 and 2 during OWLeS IOP2b (see Figure 1).

3.4. Comparison of OWLeS IOP9 to IOP7

The lake-effect band during OWLeS IOP7 also produced a line of misovortices, but across the northern band side and northern Lake Ontario. Conditions during IOP7 on 7 January 2014 (Mulholland et al., 2017) were colder (850 hPa temperatures near −25°C vs. −18°C) and had a deeper boundary layer (top ~600 hPa vs. ~800 hPa) than during IOP9 (Figure 7). Atmospheric conditions became more supportive (e.g., boundary layer deepening and moistening) of relatively strong, well-organized LLAP banding during both events when an upper-level trough approached the region during these periods of more intense banding. Both IOPs also had more intense bands during lake-to-lake (L2L) connections with Lake Huron (see Figure 3 for Lake Huron's location) and intense lake-effect band periods coincided with misovortex occurrence.

In contrast to IOP9, the IOP7 band studied by Mulholland et al. (2017) displayed misovortices on the northern band side (Figure 15). The maximum dual-Doppler-derived vertical vorticity magnitude of misovortices during IOP9 was ~6×10^{-3} s^{-1} (Figures 11 and 12) as compared to 10–30×10^{-3} s^{-1} in IOP7. The misovortices were at similar ranges from the DOWs in both IOPs and the objective analysis parameters were similar (e.g., grid spacing was 270 m in IOP9 vs. 250 m in IOP7). Thus, this difference in misovortex characteristics between the two events is likely real and not an artifact of the analysis method. The average horizontal spacing between centroids of dual-Doppler-derived vorticity maxima was 5.3 km during IOP9 vs. 6.6 km during the IOP7 event (Mulholland et al., 2017). The IOP9 misovortices were overall weaker than those during IOP7 and exhibited instances of vortex splitting (e.g., misovortex D became vortices D and F between 05:17–05:20 UTC 9 January in Figures 11b and 11c) leading to more closely spaced vortices. In contrast to IOPs 7 and 9, the median spacing between misovortices during IOP4 was 2.5–4.0 km (Kosiba et al., 2020), less than the mean spacing in both IOPs 7 and 9, but sub-snowband features, such as misovortices, were better resolved spatially in the data and analyses for IOP4 due to closer proximity to the DOW radars, and hence better azimuthal sampling. Using single Doppler

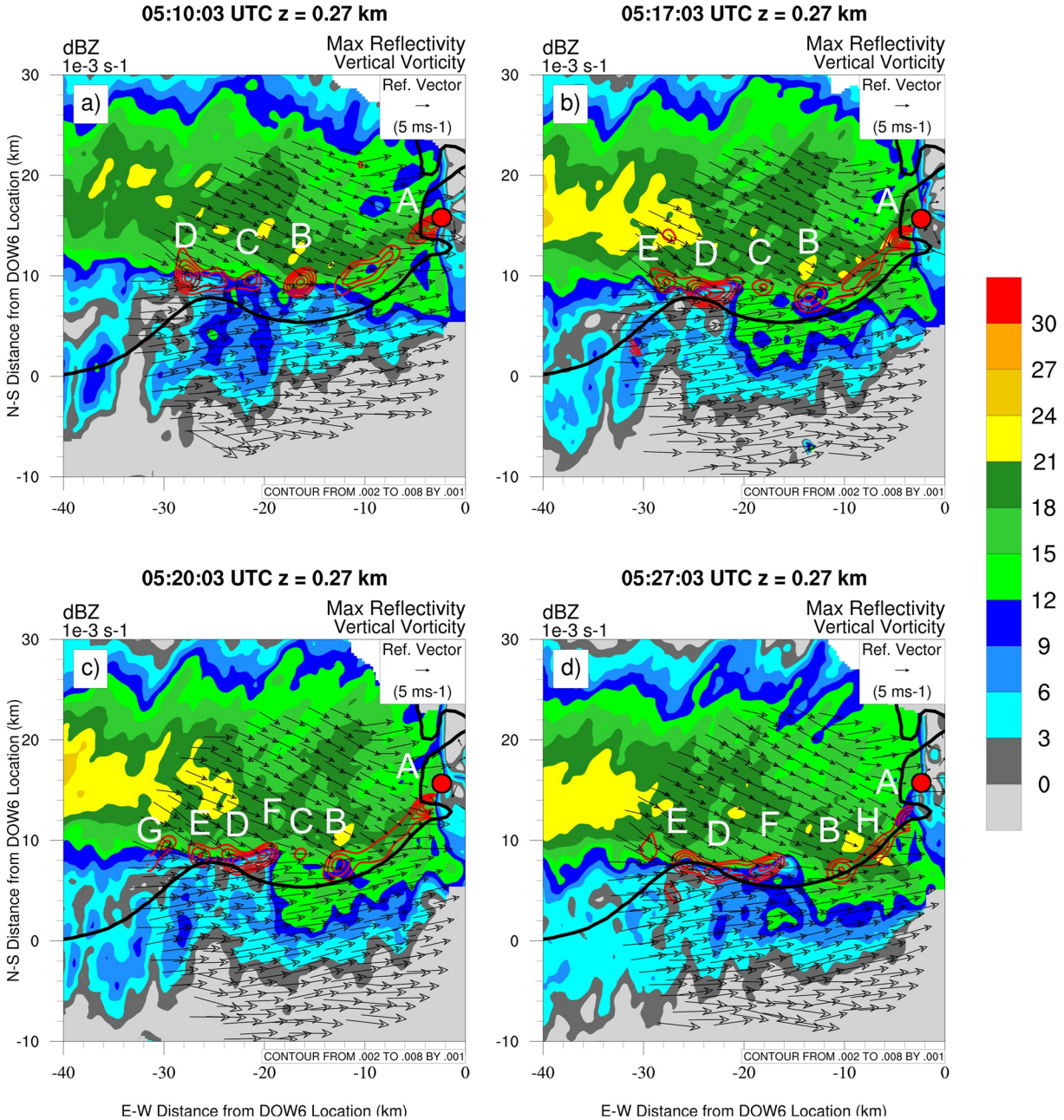

Figure 11. Time sequence of dual-Doppler derived vertical vorticity (red contours every 1×10^{-3} s^{-1} for values > 1×10^{-3} s^{-1}; letters identify individual misovortices), horizontal ground-relative winds (reference vector shown in upper right of each panel), and maximum reflectivity (dBZ; color shaded) between the two DOWs [6 at (0, 0) and 7-red dot] at 0.27 km above radar level (ARL) at (a) 05:10, (b) 05:17, (c) 05:20, and (d) 05:27 UTC 9 January 2014 (IOP9). The southeast corner of the Lake Ontario shoreline is shown as a bold black line along with the south-north and west-east distances (km) from DOW6. The area approximately corresponds with the dual-Doppler lobe shown in Figure 2.

radar observations, Kosiba et al. (2020) reported that mean/median/mode horizontal spacing between vortices from a census of 11 OWLeS IOPs were 3.2 km (standard deviation 2.0 km)/2.8 km/2.0 km. The misovortices were somewhat evenly spaced and cyclonic in line with the cyclonic horizontal shear zone during these IOPs suggesting that HSI led to their development.

The Fjørtoft's Instability Criterion (FIC; Fjørtoft, 1950), used to diagnose if an HSI was present (as done by Kosiba et al., 2020 and Mulholland et al., 2017), was calculated (across the dual-Doppler domain shown in Figure 2) and satisfied at the times and locations of the misovortices shown in Figures 11 and 12 (please see

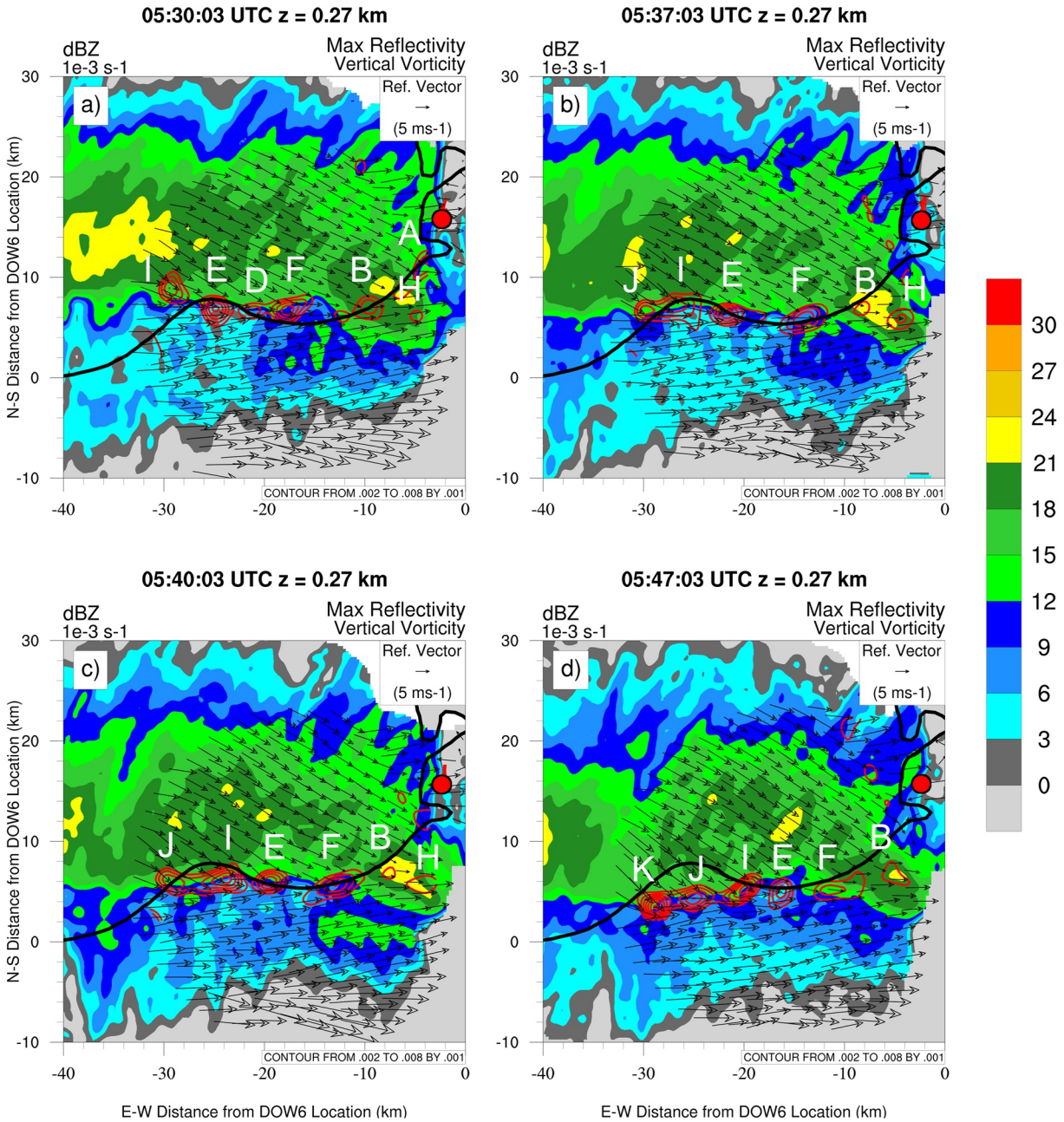

Figure 12. Same as Figure 11, but at (a) 05:30, (b) 05:37, (c) 05:40, and (d) 05:47 UTC 9 January 2014 (IOP9).

Figures S1 and S2 in Supporting Information S1) for IOP9. The weakening zonal component of the wind to the north produced the IOP9 cyclonic horizontal shear zone, as in IOP7 (Mulholland et al., 2017).

Simulated low-level convergent boundaries during IOP7 had similar shapes as the LBFs and CZ first identified during OWLeS IOP2b (Steenburgh & Campbell, 2017), but were not as well collocated with the locations of these particular boundaries as they were during IOP9, especially LBF1 (compare Figures 1, 13, and 16). The WRF simulation was inaccurate as it had the band too far south compared to reality (compare Figure 16 with Figure 5 in Mulholland et al., 2017). The convergence maximum (0.6–1 $\times 10^{-3}$ s^{-1}) was mainly across the lake center during IOP7 (Figure 16). In addition, the convergence was weaker (0.4–0.6 $\times 10^{-3}$ s^{-1}) along the LBF2 location (southeastern shore) during IOP7 vs. IOP9. Cyclonic horizontal shear occurred along boundaries in

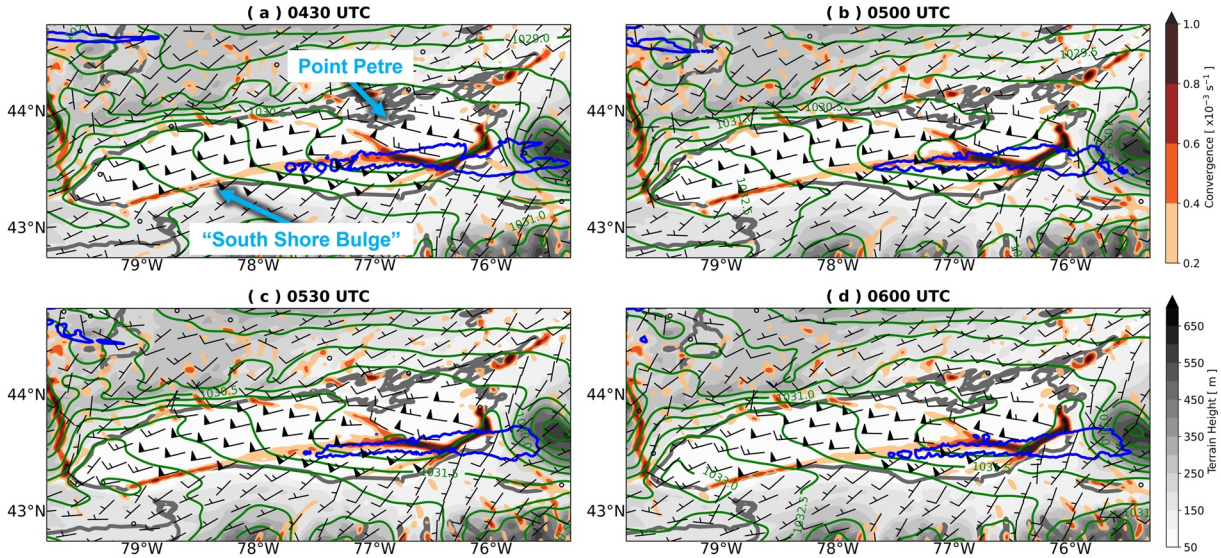

Figure 13. One kilometer WRF lowest (unstaggered) model level (~73 m AGL over Lake Ontario) convergence ($\times 10^{-3}$ s^{-1}; color shading), horizontal winds (half barb = 2.5 m s^{-1}; full barb = 5 m s^{-1}; pennant = 10 m s^{-1}), sea-level pressure (green contours every 0.5 hPa), reflectivity (blue contour = 10 dBZ), and terrain height (m; gray shading) at (a) 04:30, (b) 05:00, (c) 05:30, and (d) 06:00 UTC 9 January 2014 (IOP9). Point Petre and the "South Shore Bulge", which are referred to in the text, are labeled in panel (a).

both IOPs across eastern Lake Ontario as stronger westerly winds were south of weaker westerlies along the band. This wind pattern owes to a greater horizontal pressure gradient to the south of the band core (Figures 13 and 16).

Why did the misovortices form on the northern side of an LLAP lake-effect band during IOP7 and on the southern side of the IOP9 LLAP band? Are shear zones necessary for the formation of these misovortices as suggested by Mulholland et al. (2017)? Are boundaries such as LBFs and/or CZs necessary for these shear zones and lines of misovortices to develop? All OWLeS storm events, many of which (~50%) had misovortices, were examined next to help answer these outstanding questions.

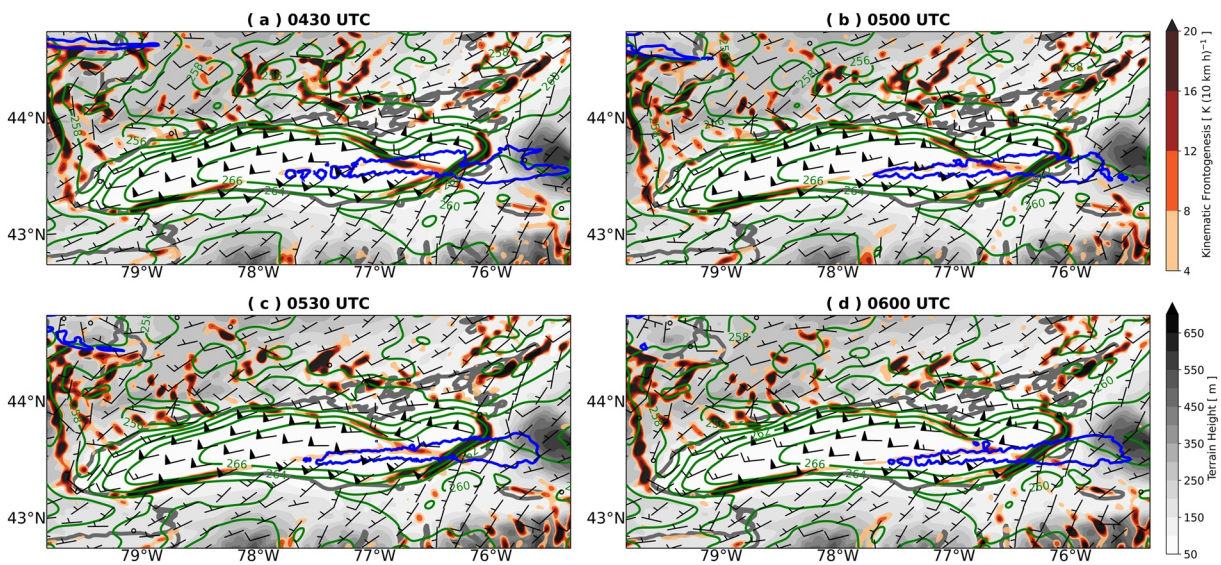

Figure 14. Same as Figure 13 except lowest (unstaggered) model level (~73 m AGL) kinematic frontogenesis (K [10 km hr]$^{-1}$; color shading) and potential temperature (green contours every 2 K) are shown.

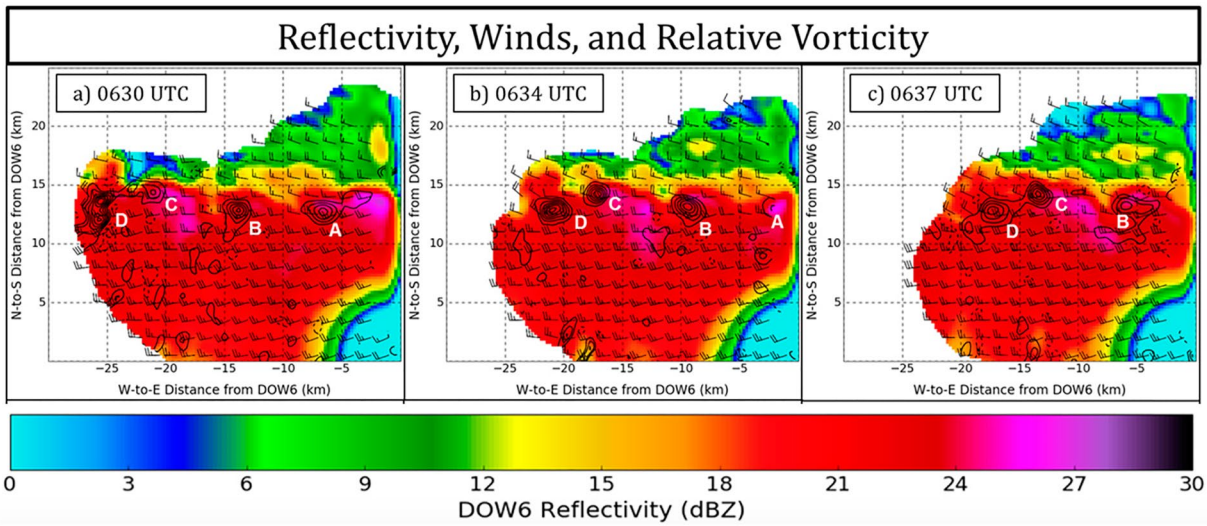

Figure 15. Dual-Doppler-derived horizontal winds (half barb = 5 m s^{-1}, full barb = 10 m s^{-1}), vertical vorticity (black contours every 5×10^{-3} s^{-1}) at 500 m AGL, and DOW6 composite reflectivity (dBZ; shaded) at (a) 06:30, (b) 06:34, and (c) 06:37 UTC 7 January 2014 (IOP7). The letters denote individual misovortices. Adapted from Figure 7 in Mulholland et al. (2017). © American Meteorological Society. Used with permission.

4. Mesoscale Band Characteristics During OWLeS Events

Radar characteristics (e.g., shear zone locations) of 23 of the 24 OWLeS IOPs (see Table 2) were investigated to determine if there were certain conditions under which misovortices occurred and the conditions when misovortices had preferred locations within the snowbands as in the case studies of IOPs 4 (Kosiba et al., 2020), 7 (Mulholland et al., 2017), and 9 (Section 3). IOP11 was not analyzed since KTYX and DOW data were unavailable.

Based upon the analysis (methods described in Section 2.3) of the lake-effect system morphology for the 23 IOPs, 11 IOPs had predominantly (i.e., at least 75% of the IOP analysis time period) LLAP characteristics (Table 2 and Figure 17, LLAP IOPs: 1, 2b, 3, 5, 7, 8, 9, 15, 21, 22, and 24). If we used at least 50% of the analysis time as our criterion in diagnosing LLAP events, two more IOPs would have been added (IOPs 4 and 6) while using a 90% criterion would have yielded two fewer events (excluding IOPs 7 and 9); hence, it is justified to use 75% as the criterion as there was not much sensitivity to this threshold and we sought events that had a characteristic for

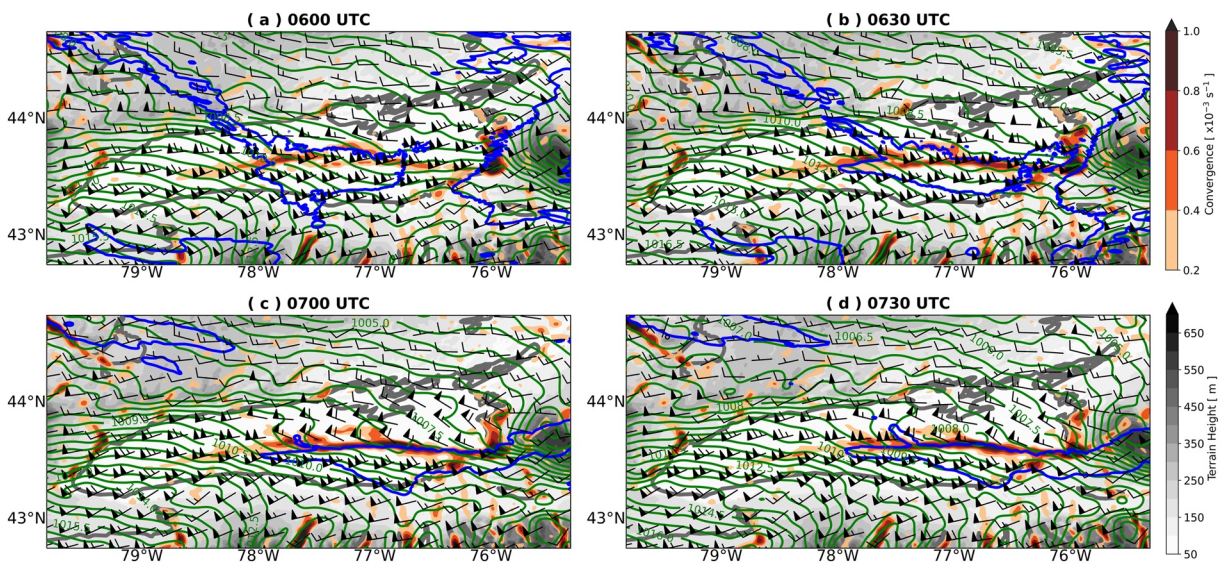

Figure 16. Same as Figure 13 except at (a) 06:00, (b) 06:30, (c) 07:00, and (d) 07:30 UTC 7 January 2014 (IOP7).

Table 2
List of Dates and Time Periods (UTC) of Analysis for All OWLeS IOPs (2013–2014)

IOP	Date and Time Period (UTC)
1	***7 December 16:00–23:00***
2a	10 December 16:40–20:20
2b	***10 December 23:00–12 December 02:00***
3	***12 December 21:00–13 December 07:00***
4	15 December 20:40–16 December 07:00
5	***18 December 16:00–19 December 00:00***
6	6 January 17:00–22:00
7	***6 January 21:00–7 January 22:30***
8	***8 January 14:00–22:00***
9	***9 January 01:00–16:00***
10	12 January 11:00–15:30
11	15 January - NA
13	18 January 22:00–19 January 00:10
14	19 January 21:00–20 January 02:00
15	***20 January 09:10–11:50***
16	21 January 17:50–22 January 00:00
17	22 January 12:00–17:00
18	23 January 17:00–24 January 03:00
19	24 January 05:00–14:00
20	26 January 12:00–20:00
21	***27 January 16:00–28 January 00:00***
22	***27 January 23:00–28 January 19:00***
23	28 January 15:00–21:30
24	***29 January 17:00–19:30***

Note. The 11 LLAP IOPs are signified by bold and italics text.

a predominant period of an event. Based on the current criterion, we identified 11 LLAP IOPs, one less than reported by Kristovich et al. (2017), whose methods for classifying LLAP events are unknown. We diagnosed IOPs 8 and 21 as LLAP that were not LLAP according to Kristovich et al. (2017), while IOPs 4, 13, and 19 were not LLAP in the current study that Kristovich et al. (2017) classified as LLAP. IOP4 was close to being classified as LLAP as 68% of the period was LLAP per Figure 17, Column 1; IOP13 only had 2 hr of radar data available to analyze out of the 5 hr total duration of the event per Table 2 in Kristovich et al. (2017); IOP19 was a shoreline band (as defined by Veals & Steenburgh, 2015). Of the 11 LLAP IOPs, 6 had major horizontal shear zones present for at least 75% of the IOP time period that we identified as LLAP (Figure 17, Column 2). One hundred percent of the LLAP period had a shear zone during IOP4, but this IOP just missed the criterion of being classified as LLAP.

The banding type for the LLAP IOPs was predominantly (≥75% of LLAP period) banded or weakly banded, except for IOPs 1 and 9 (Figure 17, Column 3). Most of the shear zone time periods also had banded structures (i.e., a solid LLAP band) during the LLAP IOPs (approximately 100% of the shear period in each IOP except for IOP9 (69%); Figure 17, Column 4). This was also true for the periods with misovortices in the LLAP IOPs (Figure 17, Column 5). There was large variability between LLAP IOPs in the percentage of shear zone periods with misovortices (Figure 17, Column 6), ranging from 0% (IOP24) to 82% (IOP15), and only two IOPs (4 and 15) in which more than 75% of the shear period had misovortices. This could be due to the radar's (DOW and/or KTYX) inability to detect and/or resolve misovortices at lower elevations (i.e., false negatives). However, the occurrence of misovortices apparently depended on shear zones as the percent of the time misovortices occurred that had shear zones (last column of Figure 17) was greater than 75% (100% for IOPs 4, 5, 7, 8, 9, 15, 21, and 22) for all LLAP IOPs in which misovortices occurred. This strongly supports the attribution by previous authors that the release of HSI instigates misovortexgenesis in LLAP bands (Kosiba et al., 2020; Mulholland et al., 2017; Steiger et al., 2013).

Horizontal shear zones formed within lake-effect bands that were near/contained low-level boundaries during portions of IOP9 (Figure 13) and IOP7 (Figure 16) that were similar in strength and position (or shape as in IOP7) to the boundaries discussed by Steenburg and Campbell (2017) during IOP2b (LBFs 1 and 2, CZ; Figure 1). The synoptic and mesoscale weather patterns of IOP2b and the other LLAP lake-effect cases, such as IOPs 7 and 9, were similar, with low-level westerly (ranging from west-southwest to west-northwest) flow across the lake, so we hypothesized that the shear zones (and misovortices) that developed during the other OWLeS LLAP cases to be associated with the boundaries diagnosed by Steenburg and Campbell (2017). Perhaps surprisingly, only 4/11 (36%) LLAP IOPs (7, 8, 22, and 24) had reflectivity bands/shear zones associated with boundaries similar to either an LBF1 or 2 or a CZ location for ≥75% of the LLAP time period (Figure 18, Column 1). Hence, one or more of the low-level boundaries similar to the LBFs/CZ are not likely to be present in Lake Ontario LLAP cases. In addition, only 6/10 (60%) LLAP IOPs (3, 7, 8, 21, 22, and 24) had at least one of these low-level boundary locations associated with a shear zone for ≥75% of the time a shear zone was present during an IOP (Figure 18, Column 2) and only 3/9 (33%) LLAP IOPs (7, 21, and 22) had a band/shear zone in an LBF/CZ location for ≥75% of the period misovortices were present (Figure 18, Column 3). Hence, convergent boundaries, such as an LBF/CZ, are not strongly associated with the strengthening of horizontal shear zones, enhanced cyclonic vertical vorticity, and misovortices in LLAP storms. Surprisingly, IOP9 had a very low percentage of the amount of time as an LLAP event, and of shear zone and misovortex time periods that a band/shear zone was associated with an LBF/CZ location (all <25%; see Figure 18, Columns 1–3). Specifically, for IOP9, only between the 05–06 UTC period were shear zones and misovortices associated with an LBF/CZ.

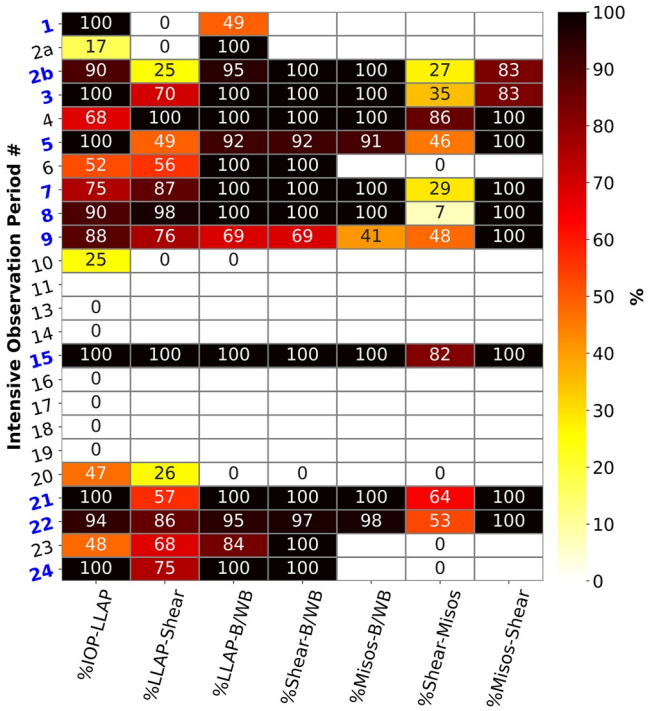

Figure 17. Heat map of: percent (%) of the IOP period that had a long lake-axis-parallel (LLAP, e.g., Figure 4a) morphology (Column 1), % of the LLAP period with a shear zone (Column 2; e.g., of an LLAP shear zone, Figure 5), % of LLAP period that had a banded/weakly banded type (B/WB, e.g., Figure 9; Column 3), % of shear period with a B/WB type (Column 4; e.g., Figure 9), % of period that had misovortices (Misos) with a B/WB type (Column 5; e.g., Figure 5a), % of shear period that had Misos (Column 6; e.g., Figure 5a), and % of Misos period that had a shear zone (Column 7; e.g., Figure 5a). The *y*-axis is the IOP number (see Table 2 for IOP date and time periods; LLAP events are blue). White regions denote where data were not available (e.g., no misovortices detected). The color shading denotes the percentage of time, with darker shading representing larger percentages.

Horizontal shear zones and misovortices had preferred locations with respect to the lake-effect band's reflectivity field in close proximity to an LBF/CZ location in several IOPs. Horizontal shear zones formed on the reflectivity band's southern side in proximity (within 5 km) to the southern shoreline of Lake Ontario during IOP9 near the boundary locations of LBFs 1 and 2 (Figures 10–12), while IOP7 had a shear zone on the band's northern side, close to the CZ boundary location (Figure 15). Lake-effect bands with shear zones that formed more toward the middle of the band and lake during OWLeS, such as during IOPs 2b and 4 (not shown), had shear zones along the LBF1 location. Based on these observations, we expected shear zones (and subsequent misovortices) forming on the north side of the band to be associated with a boundary similar to the CZ. Using ≥75% of the time a northern band shear zone existed as a benchmark, this only occurred in 2/11 (18%) IOPs (7 and 23) with available radar data (Figure 18, Column 4). One of these cases was non-LLAP (IOP23), but the association with the CZ location occurred during an LLAP period of the IOP. There was a stronger relationship between when the shear zone was on the southern side of the storm's reflectivity band and it being in the same location as LBFs 1 or 2 as 5/11 (45%) IOPs had 100% of southern band shear time associated with these LBFs (LLAP IOPs 2b, 3, 7, 21, and 22; Figure 18, Column 5). Only 4/14 (29%) total IOPs (3, 4, 15, and 21) had a high percentage of time (≥75%) when the shear zone was in the middle of the reflectivity band and associated with LBF1 (there was no expectation for a "middle" shear zone to be associated with a boundary similar to an LBF2; Figure 18, last column). Overall, there was a weak relationship between the location of shear zones relative to the band's reflectivity field and the side of the lake the band was located and the associated LBFs/CZ in these regions.

5. Discussion

Analysis of the multiple OWLeS IOPs shows that LLAP lake-effect storm misovortices depend on horizontal shear zones that form along the band's long/major axis under well-organized, banded structures. This result strongly supports that HSI is a prerequisite for misovortexgenesis in LLAP lake-effect storms, as shown for IOPs 4 (Kosiba et al., 2020), 7 (Mulholland et al., 2017), and 9 herein. To objectively confirm this statement, however, HSI criteria such as Fjørtoft's Instability Criterion (FIC) calculated using airflow determined from dual-Doppler and/or WRF simulations of all LLAP lake-effect storms during OWLeS would have to be conducted, which is left as future work.

This study provides evidence for the hypothesis that boundaries similar to LBFs and the CZ (Steenburgh & Campbell, 2017), in the presence of an enhanced north-to-south horizontal pressure gradient (e.g., that leads to stronger westerly winds on the band's south side, e.g., Figure 13), can serve as the source of horizontal shear zones and can also provide the vertically oriented vorticity needed to initiate/strengthen the misovortices (i.e., create HSI as discussed by Steiger et al., 2013 and references therein [e.g., Lee & Wilhelmson, 1997]). This connection to LBFs and the CZ was more evident in shear zones that formed on the southern band side near the south shore of Lake Ontario (e.g., during the periods shown in Figures 11 and 12 during IOP9). For example, the schematic in Figure 19 shows how a boundary's (similar to LBF2) convergence (and the updrafts within the band itself) collocated with cyclonic horizontal shear can lead to stretching of the vertical vorticity maxima formed by the horizontal shear zone and the release of HSI on the south side of an LLAP band similar to that during IOP9 (Figures 9, 11, and 12). The horizontal shear zone is set up by the low-level pressure distribution that develops in response to the synoptic pattern conducive to LLAP band development (i.e., low pressure to the north/northeast that occurred for all LLAP IOPs in this study) and smaller-scale pressure patterns which occur underneath areas of maximum heating owing to sensible heat fluxes off of Lake Ontario and sensible and latent heat fluxes within the band. The pressure distribution depicted in Figure 19 is supported by the pressure (Figure 13) and kinematic frontogenesis (Figure 14) analyses from the IOP9 WRF simulation, which supports that the shear zone formed on an LBF similar to LBF2.

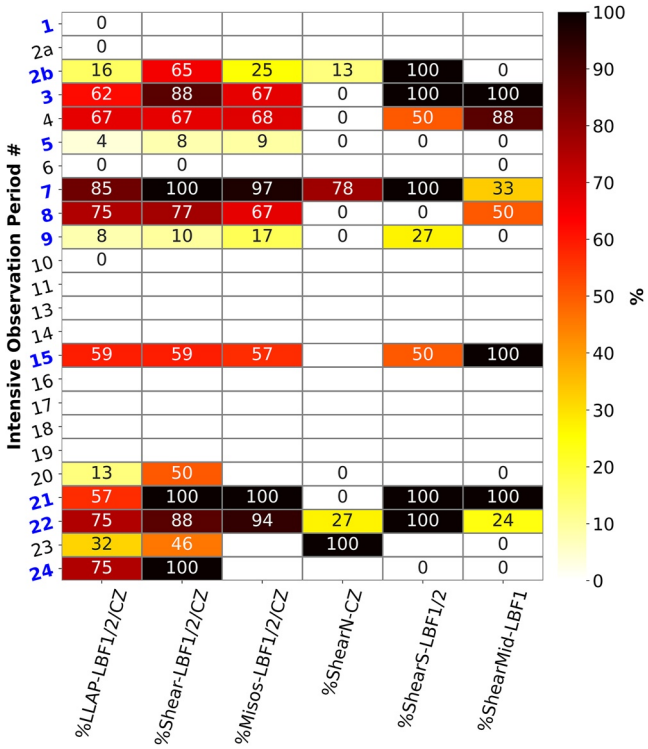

Figure 18. Heat map of: percent (%) of the long lake-axis-parallel (LLAP) morphology time period that had a reflectivity band/horizontal shear zone associated with a boundary similar to the land breeze front (LBF1 or 2) or convergence zone (CZ) location identified by Steenburgh and Campbell (2017) (Column 1), % of the shear zone period that had this association (Column 2), % of the period exhibiting misovortices (Misos) that had this association (Column 3), % of the period when a shear zone was on the north (N) side of the band that was associated with a boundary similar to the CZ (Column 4), % of the period when a shear zone was on the south (S) side of the band that was associated with a boundary similar to an LBF1/2 (Column 5), and % of the period when a shear zone was in the middle of the band that was associated with a boundary similar to an LBF1 (Column 6). The *y*-axis is the IOP number (see Table 2 for IOP date and time periods; LLAP IOPs are blue). White regions denote where data were not available (e.g., no misovortices detected). The color shading denotes the percentage of time, with darker shading representing larger percentages.

The association between a shear zone on the south side of a band and forming on/near the location of LBF1 or 2 (on the south side of the lake) is weak, even for IOP9 as this occurred only 27% of the time a south side shear zone formed during this IOP (Figure 18, Column 5). The majority (6/11 or 55%) of IOPs where shear zones formed on the south side of a band were not associated with the LBFs 1 or 2 (Figure 18, Column 5; IOPs 4, 5, 8, 9, 15, and 24). More relatively frequent cases occurred when northern lake band shear zones were not associated with a boundary similar to a CZ (Figure 18, Column 4; IOPs 2b, 3–5, 8, 9, and 20–22). One hypothesis is that these shear zones formed along low-level boundaries that were internally generated as discussed by Kosiba et al. (2020) during IOP4. For example, sublimation-driven cold pools can develop outflow boundaries in the bands. If cold pool-generated boundaries occurred, we expected to see radar-detected shear zones and boundaries move away from the band reflectivity core as the storm's outflow evolved and deepened (e.g., 4–5 January 2011 case in Steiger et al., 2013). This was not observed for any of the LLAP cases during our radar analysis. However, boundaries can be stalled as they interact with the environmental wind shear. Hence, the cause of the horizontal shear zones and subsequent misovortices that occurred in these particular LLAP cases is unknown and requires further study.

6. Conclusions

Kosiba et al. (2020) and Mulholland et al. (2017) show strong support for HSI as the primary mechanism for LLAP lake-effect band misovortex development for the OWLeS cases of IOP4 and IOP7, respectively. In Mulholland et al. (2017), the line of misovortices was on the northern side of the zonally oriented band, while in Kosiba et al. (2020) the misovortices were on either side, but predominantly on the southern side of the band (note the vortex line in their case was affected by an arctic front interacting with the lake band toward the end of IOP4). We show similar lines of misovortices to as in these cases of HSI-induced misovortices during IOP9, but unlike Mulholland et al. (2017) and like Kosiba et al. (2020), this line occurred on the southern side of the zonal band.

The IOP9 shear zone upon which these misovortices formed developed on a land breeze-type front. The misovortices documented in IOP9 had weaker vertical vorticity than documented in IOP7 and IOP4 (and less than the median inferred vertical vorticity for all LLAP cases in Kosiba et al., 2020). These similarities and differences led to an expansion of our analysis of misovortices and their parent shear zones in other OWLeS cases. We focused on 11 LLAP band cases and discovered the following:

- About half (6/11; 55%) of OWLeS LLAP IOPs had shear zones within them for a large portion of the LLAP time period (≥75% of the time) and all, but one of these six IOPs had identified misovortices (5/6; 83%). Shear zones and misovortices were strongly dependent on the LLAP storm having a banded mode.
- Reflectivity bands or shear zones and misovortices developed near convergence zones (LBFs 1 or 2, CZ) associated with Lake Ontario geographical features first identified by Steenburg and Campbell (2017) in several (but a minority) of the OWLeS IOPs (4/11 or 36% of LLAP IOPs and 3/9 or 33% of misovortex LLAP IOPs had bands/shear zones strongly associated with these features), and the locations of the shear zones and misovortices within the reflectivity band had a preferred in-band location (i.e., southern/northern side) and were linked to a boundary similar to a CZ/LBF in a minority (5/11 or 45% for southern side, 2/11 or 18% for northern side) of OWLeS IOPs. Hence, our hypothesis that shear zones and lines of misovortices within

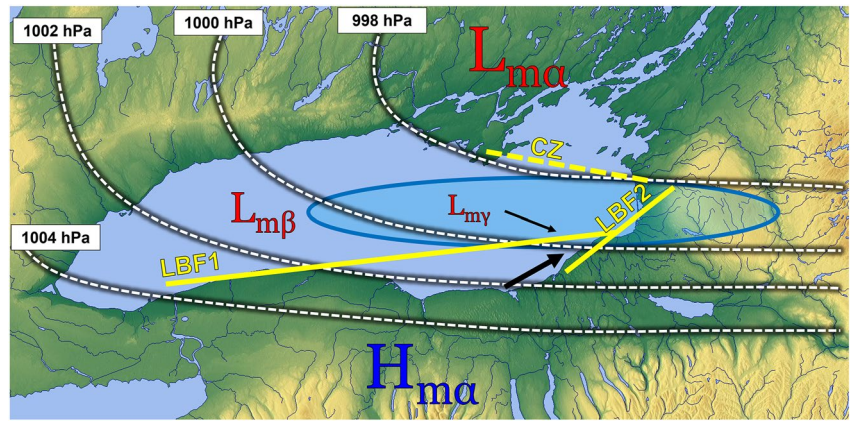

Figure 19. Schematic showing the positions of the meso-alpha- (subscript "mα"), meso-beta- (subscript "mβ"), and meso-gamma-scale (subscript "mγ") (Fujita, 1981) pressure areas (H, high; L, low), representative isobars (white dashed lines), lake-effect ≥10 dBZ reflectivity band (shaded and contoured in blue), boundaries similar to LBF1/2 and CZ (yellow lines) from Steenburg and Campbell (2017), and vectors representing near surface horizontal wind (black arrows with the arrow size representing relative magnitudes) for a case similar to IOP9 (based on Figures 11 and 13 of this paper, Figure 19 in Mulholland et al., 2017 and Steenburgh & Campbell, 2017). The meso-β- and meso-γ-scale low pressure areas extend along the long axis of the lake and band, respectively, and when combined with the meso-α-scale pressure distribution leads to the isobar pattern shown. Map from maps-for-free.com.

LLAP bands are formed via processes related to the Steenburg and Campbell (2017)-type boundaries is not well-supported.

Figure 19 represents a plausible hypothesis for the development of horizontal shear zones and lines of misovortices forming along the southern side of an LLAP band (e.g., during portions of IOP9) associated with the LBF2 boundary location. The surface pressure distribution around the band supports the development of stronger westerly winds to the south of the band's core leading to low-level cyclonic shear vorticity and the development of an HSI if favorably perturbed. A boundary similar to LBF2 lifts the air via enhanced low-level convergence, fostering heavier snowfall production (e.g., boosting radar reflectivity) and updrafts enhance vertical vorticity maxima (misovortices) via vortex stretching along the southern band side.

Future work requires study of the cases when shear zones and misovortex lines form within LLAP lake-effect bands not associated with the boundaries focused on in this study (LBFs 1 or 2, and CZ). We plan to develop and use more objective methods, such as specific quantitative thresholds for identifying shear zones, and an objective method to determine the strength of many misovortices without needing to perform dual-Doppler analysis of all IOPs. Outstanding questions from this work include: Why did the IOP9 misovortices have weaker vertical vorticity and were spaced closer to each other as compared to those in IOP7? Were there environmental factors and/or storm-scale processes that caused these differences, or were they determined by the characteristics of the low-level horizontal shear zone?

Data Availability Statement

To obtain the full list of data and scripts used in this paper, please visit https://figshare.com/account/home%23/projects/146067. Additionally, NCAR-EOL specifically maintains the OWLeS data repository (see https://data.eol.ucar.edu/master_list/?project=OWLeS for access to the DOW and sounding data used in this paper).

Acknowledgments
Kudos to all of the OWLeS participants for their hard work and dedication in collecting (in sometimes very harsh conditions) so much relevant data to work with. The authors thank Brianna Bealo for her work that led to some of the methods used in identifying LLAP bands, shear zones, and misovortices with radar data. The material is based upon work supported by the National Science Foundation (NSF) under Grant AGS-1258894.

References

Barnes, S. L. (1964). A technique for maximizing details in numerical weather map analysis. *Journal of Applied Meteorology and Climatology*, *3*(4), 396–409. https://doi.org/10.1175/1520-0450(1964)003<0396:atfmdi>2.0.co;2

Bergmaier, P. T., & Geerts, B. (2020). LLAP band structure and intense lake-effect snowfall downwind of Lake Ontario: Insights from the OWLeS 7–9 January 2014 event. *Journal of Applied Meteorology and Climatology*, *59*(10), 1691–1715. https://doi.org/10.1175/jamc-d-19-0288.1

Bergmaier, P. T., Geerts, B., Campbell, L. S., & Steenburgh, W. J. (2017). The OWLeS IOP2b lake-effect snowstorm: Dynamics of the secondary circulation. *Monthly Weather Review*, *145*(7), 2437–2459. https://doi.org/10.1175/MWR-D-16-0462.1

Campbell, L. S., Steenburgh, W. J., Veals, P. G., Letcher, T. W., & Minder, J. R. (2016). Lake-effect mode and precipitation enhancement over the Tug Hill plateau during OWLeS IOP2b. *Monthly Weather Review*, *144*(5), 1729–1748. https://doi.org/10.1175/MWR-D-15-0412.1

Center for Severe Weather Research (CSWR). (2020). About the DOWs. Retrieved from http://www.cswr.org/contents/aboutdows.php

Fjørtoft, R. (1950). Application of integral theorems in deriving criteria of stability for laminar flows and for the baroclinic circular vortex. *Geofysiske Publikasjoner*, *17*(6), 1–52.

Fujita, T. T. (1981). Tornadoes and downbursts in the context of generalized planetary scales. *Journal of the Atmospheric Sciences*, *38*(8), 1511–1534. https://doi.org/10.1175/1520-0469(1981)038<1511:taditc>2.0.co;2

Fujiwhara, S. (1931). Short note on the behavior of two vortices. *Proceedings of the Physico—Mathematical Society of Japan. 3rd Series*, *13*(3), 106–110. https://doi.org/10.11429/ppmsj1919.13.3_106

Great Lakes Environmental Research Lab (GLERL). (2022). Data and products. Retrieved 14 July 2021 from https://www.glerl.noaa.gov/data/

Iacono, M. J., Delamere, J. S., Mlawer, E. J., Shephard, M. W., Clough, S. A., & Collins, W. D. (2008). Radiative forcing by long-lived greenhouse gases: Calculations with the AER radiative transfer models. *Journal of Geophysical Research: Atmospheres*, *113*(D13103). https://doi.org/10.1029/2008JD009944

Jiménez, P. A., Dudhia, J., González-Rouco, J. F., Navarro, J., Montávez, J. P., & García-Bustamante, E. (2012). A revised scheme for the WRF surface layer formulation. *Monthly Weather Review*, *140*(3), 898–918. https://doi.org/10.1175/MWR-D-11-00056.1

Kosiba, K. A., Wurman, J., Knupp, K., Pennington, K., & Robinson, P. (2020). Ontario Winter Lake-effect Systems (OWLeS): Bulk characteristics and kinematic evolution of misovortices in long-lake-axis-parallel snowbands. *Monthly Weather Review*, *148*(1), 131–157. https://doi.org/10.1175/MWR-D-19-0182.1

Kosiba, K. A., Wurman, J., Richardson, Y., Markowski, P., Robinson, P., & Marquis, J. (2013). Genesis of the Goshen County, Wyoming, tornado on 5 June 2009 during VORTEX2. *Monthly Weather Review*, *141*(4), 1157–1181. https://doi.org/10.1175/MWR-D-12-00056.1

Kristovich, D. A. R., Clark, R. D., Frame, J., Geerts, B., Knupp, K. R., Kosiba, K. A., et al. (2017). The Ontario Winter Lake-effect Systems field campaign: Scientific and education adventures to further our knowledge and prediction of lake-effect storms. *Bulletin of the American Meteorological Society*, *98*(2), 315–332. https://doi.org/10.1175/BAMS-D-15-00034.1

Kristovich, D. A. R., & Steve, R. A., III. (1995). A satellite study of cloud-band frequencies over the Great Lakes. *Journal of Applied Meteorology and Climatology*, *34*(9), 2083–2090. https://doi.org/10.1175/1520-0450(1995)034<2083:assocb>2.0.co;2

Lee, B. D., & Wilhelmson, R. B. (1997). The numerical simulation of non-supercell tornadogenesis. Part I: Initiation and evolution of pretornadic misocyclone circulations along a dry outflow boundary. *Journal of the Atmospheric Sciences*, *54*(1), 32–60. https://doi.org/10.1175/1520-0469(1997)054<0032:tnsons>2.0.co;2

Majcen, M., Markowski, P., Richardson, Y., Dowell, D., & Wurman, J. (2008). Multipass objective analysis of Doppler radar data. *Journal of Atmospheric and Oceanic Technology*, *25*(10), 1845–1858. https://doi.org/10.1175/2008JTECHA1089.1

Mulholland, J. P., Frame, J., Nesbitt, S. W., Steiger, S. M., Kosiba, K. A., & Wurman, J. (2017). Observations of misovortices within a long-lake-axis-parallel lake-effect snowband during the OWLeS project. *Monthly Weather Review*, *145*(8), 3265–3291. https://doi.org/10.1175/MWR-D-16-0430.1

National Center for Environment Information (NCEI). (2022). *NOAA's weather and climate toolkit*. NOAA. Retrieved from https://www.ncdc.noaa.gov/wct/

Niziol, T. A., Snyder, W. R., & Waldstreicher, J. S. (1995). Winter weather forecasting throughout the eastern United States. Part IV: Lake effect snow. *Weather and Forecasting*, *10*(1), 61–77. https://doi.org/10.1175/1520-0434(1995)010<0061:wwftte>2.0.co;2

Pauley, P. M., & Wu, X. (1990). The theoretical, discrete, and actual response of the Barnes objective analysis scheme for one- and two-dimensional fields. *Monthly Weather Review*, *118*(5), 1145–1164. https://doi.org/10.1175/1520-0493(1990)118<1145:ttdaar>2.0.co;2

Peace, R. L., Jr., & Sykes, R. B., Jr. (1966). Mesoscale study of a lake effect snowstorm. *Monthly Weather Review*, *94*(8), 495–507. https://doi.org/10.1175/1520-0493(1966)094<0495:msoale>2.3.co;2

Shin, H. H., & Hong, S.-Y. (2015). Representation of the subgrid-scale turbulent transport in convective boundary layers at gray-zone resolutions. *Monthly Weather Review*, *143*(1), 250–271. https://doi.org/10.1175/MWR-D-14-00116.1

Skamarock, W. C., Klemp, J. B., Dudhia, J., Gill, D. O., Barker, D., Duda, M. G., et al. (2008). A description of the Advanced Research WRF version 3. NCAR Tech. Note NCAR/TN-475+STR, (p. 113). 10.5065/D68S4MVH

Steenburgh, W. J., & Campbell, L. S. (2017). The OWLeS IOP2b lake-effect snowstorm: Shoreline geometry and the mesoscale forcing of precipitation. *Monthly Weather Review*, *145*(7), 2421–2436. https://doi.org/10.1175/MWR-D-16-0460.1

Steiger, S. M., Kranz, T., & Letcher, T. W. (2018). Thunderstorm characteristics during the Ontario Winter Lake-Effect Systems project. *Journal of Applied Meteorology and Climatology*, *57*(4), 853–874. https://doi.org/10.1175/JAMC-D-17-0188.1

Steiger, S. M., Schrom, R., Stamm, A., Ruth, D., Jaszka, K., Kress, T., et al. (2013). Circulations, bounded weak echo regions, and horizontal vortices observed within long-lake-axis-parallel-lake-effect storms by the Doppler on Wheels. *Monthly Weather Review*, *141*(8), 2821–2840. https://doi.org/10.1175/MWR-D-12-00226.1

Thompson, G., Field, P. R., Rasmussen, R. M., & Hall, W. D. (2008). Explicit forecasts of winter precipitation using an improved bulk microphysics scheme. Part II: Implementation of a new snow parameterization. *Monthly Weather Review*, *136*(12), 5095–5115. https://doi.org/10.1175/2008MWR2387.1

Veals, P. G., & Steenburgh, W. J. (2015). Climatological characteristics and orographic enhancement of lake-effect precipitation east of Lake Ontario and over the Tug Hill plateau. *Monthly Weather Review*, *143*(9), 3591–3609. https://doi.org/10.1175/MWR-D-15-0009.1

Wurman, J., & Kosiba, K. (2018). FARM-data-OWLES (Version 1) [Dataset]. Center for Severe Weather Research. https://doi.org/10.48514/29DT-ZA28

Wurman, J., Kosiba, K., Pereira, B., Robinson, P., Frambach, A., Gilliland, A., et al. (2021). The FARM (Flexible Array of Radars and Mesonets). *Bulletin of the American Meteorological Society*, *102*(8), E1499–E1525. https://doi.org/10.1175/BAMS-D-20-0285.1